TTP21-031
P3H-21-065

Tasting Flavoured Majorana Dark Matter

Harun Acaroğlu[a], Monika Blanke[a,b]

[a] *Institut für Theoretische Teilchenphysik, Karlsruhe Institute of Technology, Engesserstraße 7, D-76128 Karlsruhe, Germany*

[b] *Institut für Astroteilchenphysik, Karlsruhe Institute of Technology, Hermann-von-Helmholtz-Platz 1, D-76344 Eggenstein-Leopoldshafen, Germany*

Abstract

We study a simplified model of flavoured Majorana dark matter in the Dark Minimal Flavour Violation framework. The model extends the Standard Model by a dark matter flavour triplet and a scalar mediator, through which the new dark fermions couple to right-handed up-type quarks. This interaction is governed by a new coupling matrix λ which is assumed to constitute the only new source of flavour and CP violation. We analyse the parameter space of this model by using constraints from collider searches, $D^0 - \bar{D}^0$ mixing, cosmology and direct dark matter searches. Throughout our study, we point out crucial differences between the Majorana and Dirac dark matter cases. After performing a combined analysis within the context of all the experimental constraints mentioned above, we analyse which flavour for the dark matter particle is preferred by experimental data. We further investigate if this model is capable of explaining the large measured value of the direct CP asymmetry $\Delta A_{CP}^{\rm dir}$ in charm decays. We find that significant enhancements with respect to the Standard Model expectation are compatible with all constraints, and in one benchmark scenario even the central value of the measurement can be reached. We also advertise the flavour-violating final state with two same-sign top quarks produced in association with missing transverse energy as a smoking-gun signature for flavoured Majorana dark matter at the LHC.

Contents

1 Introduction **3**

2 Flavoured Majorana Dark Matter in DMFV **4**
2.1 A Simplified DMFV Model 4
2.2 Parametrization of the DM-Quark Coupling λ 5
2.3 Mass Spectrum and Dark Matter Stability 6

3 Collider Phenomenology **7**
3.1 LHC Signatures from Mediator Pair-Production 8
3.2 Recast of LHC Constraints 9
3.3 Same-sign tops at the LHC 12

4 Flavour Physics Phenomenology **13**
4.1 Neutral D Meson Mixing 13
4.2 Application of the D meson mixing constraints 15

5 Cosmological Implications **18**
5.1 DM Annihilation and Freeze-Out Scenarios 18
5.2 Analysis of the Relic Abundance Constraints 20

6 Dark Matter Phenomenology **23**
6.1 DM-Nucleon Scattering Processes 23
6.2 Direct Detection Constraints 25

7 Combined Analysis **27**
7.1 Combined Constraints 27
7.2 What's your flavour? Tell me, what's your flavour? 29

8 Direct CP Violation in Charm Decays **30**
8.1 Theoretical Approach 31
8.2 Results 33

9 Summary and Outlook **34**

A Direct Detection **37**
A.1 Gluonic Wilson Coefficients 37

1 Introduction

Despite the overwhelming astrophysical and cosmological evidence for the existence of dark matter (DM), its particle nature remains obscure. With the non-observation of DM particles in direct detection experiments and at the LHC, the WIMP paradigm – i. e. a weakly-coupled DM particle with weak-scale mass – has been put under severe pressure [1]. As a consequence, alternatives to the simple WIMP scenario have become increasingly popular.

One possibility to reconcile the WIMP paradigm with experimental data is the introduction of an extended dark sector in which the DM candidate carries charge under a flavour symmetry [2–10]. While the first studies of such flavoured DM models were confined to the Minimal Flavour Violation (MFV) [11–15] hypothesis, more recently the concept of flavoured DM with a non-trivial flavour structure has been put forward [16–20]. In this case the coupling between the DM flavour multiplet and the Standard Model (SM) fermions constitutes a new source of flavour and CP violation, so that the phenomenology vastly changes with respect to the MFV-type models.

In order to systematically study the phenomenological implications of such a non-MFV coupling between DM and the SM, the concept of Dark Minimal Flavour Violation (DMFV) has been introduced [16]. Conceptually similar to the MFV hypothesis, in DMFV models the coupling between the DM flavour triplet and the SM quark or lepton flavour triplet is assumed to be the only new source of flavour and CP violation beyond the SM Yukawa couplings. The assumption of DMFV has the advantage of keeping the number of parameters in the simplified models minimal and thus allowing for an efficient study of their rich phenomenology.

Previous analyses of simplified models with DMFV introduced DM as a Dirac fermion transforming as a triplet under a new $U(3)_\chi$ flavour symmetry, either coupling to the SM down-type quarks [16], up-type quarks [17,18], left-handed quark doublets [19] or charged leptons [20] via a scalar mediator. In the present paper we instead explore the possibility to introduce the DM flavour triplet as a Majorana fermion. Since the Majorana nature requires the DM to transform under a real representation, we take the flavour symmetry in the dark sector to be $O(3)_\chi$, instead of $U(3)_\chi$ in the Dirac case.

As a benchmark case, we consider the case of flavoured Majorana DM in which the dark flavour triplet χ couples to the right-handed up-type quarks, in analogy to the Dirac DM model studied in [17,18]. To allow for a straightforward comparison of the phenomenology of the two models, let us briefly recall the main results of [17]:

- The stringent constraints from $D^0 - \bar{D}^0$ mixing required a strong suppression of flavour changing neutral current (FCNC) processes, thereby forbidding interesting non-standard effects in rare and CP-violating D meson decays.

- The LHC experiments ATLAS and CMS put lower bounds on the mass of the scalar mediator, depending on the DM mass and the coupling strength to SM quarks. The strongest constraints arise from searches for final states with jets plus missing transverse energy $\not{E}_T$.

- Similarly to flavour-violating supersymmetric models [21, 22], the model predicts the new benchmark signatures $tj + \not{E}_T$ and monotop+$\not{E}_T$ at a significant rate. A dedicated experimental search has been proposed in [23].

- The limits from direct detection experiments severely constrain the allowed ranges of DM-quark couplings, requiring a destructive interference between the various tree- and

loop-level contributions to the DM-nucleon scattering cross section. In combination with the constraints from the thermal freeze-out condition, the direct detection limits translate into a lower bound on the DM mass.

Analysing the constraints from collider searches, flavour physics, cosmology and direct detection experiments, we shall see that the phenomenology changes drastically when, instead of a Dirac fermion, DM is introduced as a Majorana fermion.

2 Flavoured Majorana Dark Matter in DMFV

The subject of this paper is a simplified model based on the DMFV hypothesis [16]. This section briefly introduces the DMFV framework in general and then presents the explicit DMFV model to be studied.

2.1 A Simplified DMFV Model

In the DMFV framework the SM is extended by a new flavour symmetry, generically denoted as $\mathcal{G}_\chi(3)$, and a DM field χ, that transforms under the fundamental representation of this new symmetry. This results in a global

$$\mathcal{G}_{\text{DMFV}} = U(3)_q \times U(3)_u \times U(3)_d \times \mathcal{G}(3)_\chi \tag{2.1}$$

flavour symmetry, where we focus on DM interacting with SM quarks. Depending on whether the field χ is a Dirac or Majorana fermion the symmetry group $\mathcal{G}(3)_\chi$ is either a $U(3)_\chi$ or an $O(3)_\chi$ group, respectively. In DMFV the SM Yukawa couplings Y_u, Y_d, and λ – the coupling of χ to quarks – constitute the only sources that break the flavour symmetry $\mathcal{G}_{\text{DMFV}}$. In this sense, the DMFV framework goes beyond the scope of MFV [11–15], as it extends the SM flavour symmetry by $\mathcal{G}(3)_\chi$ and includes one new source of flavour and CP violation, namely λ. DMFV models can be classified by the type of flavour to which the DM couples and the fermion nature of the DM particle. The cases of χ being a Dirac fermion and coupling to right-handed up quarks u_R [17, 18], right-handed down quarks d_R [16], left-handed quark doublets q_L [19] and right-handed charged leptons [20] have already been studied.

In this paper we present a simplified model that constitutes the first realization of the DMFV ansatz where the new DM field χ is assumed to be a Majorana fermion. In analogy to the model analysed in [17], it is assumed that χ couples to right-handed up quarks through the exchange of a scalar boson ϕ. The Lagrangian of this model reads:

$$\begin{aligned}\mathcal{L} = \mathcal{L}_{\text{SM}} + \frac{1}{2}\left(i\bar{\chi}\partial\!\!\!/\chi - M_\chi\bar{\chi}\chi\right) - \left(\lambda_{ij}\,\bar{u}_{Ri}\chi_j\,\phi + h.c.\right) + (D_\mu\phi)^\dagger(D^\mu\phi) \\ - m_\phi^2\,\phi^\dagger\phi + \lambda_{H\phi}\,\phi^\dagger\phi\,H^\dagger H + \lambda_{\phi\phi}\left(\phi^\dagger\phi\right)^2 .\end{aligned} \tag{2.2}$$

Here we have introduced χ as a four-component Dirac spinor $\chi = (\chi_L, i\sigma_2\chi_L^*)^T$, with χ_L being a two-component Weyl spinor. Note that due to its Majorana nature the kinetic term and the mass term of χ include a factor of $1/2$. The field χ transforms as a singlet under the SM gauge group and as a triplet under a global $O(3)_\chi$ symmetry, i.e. it comes in three generations. Its lightest generation is assumed to constitute the observed DM in the universe. Interactions between SM quarks and this new DM field χ are parametrised by the coupling

λ, a general complex 3×3 matrix. This interaction is mediated by the scalar boson ϕ which carries hypercharge and colour. The couplings $\lambda_{H\phi}$ and $\lambda_{\phi\phi}$ have no relevance for our analysis and are only mentioned for completeness.

2.2 Parametrization of the DM-Quark Coupling λ

In order to analyse the constraints on our model we need to first parametrise the physical degrees of freedom in the flavour sector. For the Yukawa couplings Y_u and Y_d one can proceed as usual and use the SM flavour symmetry in order to remove unphysical parameters to finally end up with six quark masses and the CKM matrix.

A similar procedure has to be performed for the new coupling λ. According to the DMFV ansatz λ is an arbitrary complex 3×3 matrix. Therefore it contains 18 parameters, consisting of 9 real parameters and 9 complex phases. In the following we want to make use of the flavour symmetry $\mathcal{G}_{\text{DMFV}}$ and the symmetry $O(3)_\chi$ in particular in order to remove unphysical degrees of freedom from λ.

As a first step λ is expressed through a singular value decomposition, yielding

$$\lambda = U_\lambda D_\lambda V_\lambda \,. \tag{2.3}$$

Here, U_λ and V_λ are unitary matrices and D_λ is a diagonal matrix with positive and real entries. Taking into account that eq. (2.3) is invariant under the diagonal rephasing

$$\begin{aligned} U'_\lambda &= U_\lambda \,\text{diag}(e^{i\alpha_1}, e^{i\alpha_2}, e^{i\alpha_3}) \,, \\ V'_\lambda &= \text{diag}(e^{-i\alpha_1}, e^{-i\alpha_2}, e^{-i\alpha_3})\, V_\lambda \,, \end{aligned} \tag{2.4}$$

this parametrization indeed contains 9 real parameters and 9 complex phases.

One can now use the flavour symmetry $\mathcal{G}_{\text{DMFV}}$ in order to remove more unphysical degrees of freedom from λ. Note that for the case of χ being a Dirac fermion $\mathcal{G}_{\text{DMFV}}$ contains a $U(3)_\chi$ symmetry. In such models the flavour symmetry of χ can thus be used to fully remove the unitary matrix V_λ and end up with $\lambda = U_\lambda D_\lambda$ [16, 17, 19]. For our case of a Majorana fermion χ the Lagrangian is no longer invariant under such $U(3)_\chi$ transformations, since Majorana fields can only transform under real representations. Indeed the bilinear

$$\bar{\chi}\chi = i(\chi_L^\dagger \sigma_2 \chi_L^* - \chi_L^T \sigma_2 \chi_L) \,. \tag{2.5}$$

is only invariant under orthogonal transformations. Thus, one is left with an $O(3)_\chi$ symmetry that can be used to remove 3 real degrees of freedom from V_λ.

According to [24] the unitary matrix V_λ can be decomposed as

$$V_\lambda = O_V \, d_V \, P_V \,. \tag{2.6}$$

Here, O_V and P_V are orthogonal matrices with 3 real degrees of freedom and d_V is a diagonal unitary matrix with 3 complex phases. The orthogonal matrix P_V can now be removed from V_λ by using the transformation

$$\chi \to P_V^{-1} \chi \,. \tag{2.7}$$

This finally yields

$$\lambda = U \, D \, O \, d \,, \tag{2.8}$$

where we have omitted the indices for brevity of notation.

We adopt the parametrisation for U from [17, 25], which reads

$$\begin{aligned} U &= U_{23}\, U_{13}\, U_{12} \\ &= \begin{pmatrix} 1 & 0 & 0 \\ 0 & c_{23}^{\theta} & s_{23}^{\theta} e^{-i\delta_{23}} \\ 0 & -s_{23}^{\theta} e^{i\delta_{23}} & c_{23}^{\theta} \end{pmatrix} \begin{pmatrix} c_{13}^{\theta} & 0 & s_{13}^{\theta} e^{-i\delta_{13}} \\ 0 & 1 & 0 \\ -s_{13}^{\theta} e^{i\delta_{13}} & 0 & c_{13}^{\theta} \end{pmatrix} \begin{pmatrix} c_{12}^{\theta} & s_{12}^{\theta} e^{-i\delta_{12}} & 0 \\ -s_{12}^{\theta} e^{i\delta_{12}} & c_{12}^{\theta} & 0 \\ 0 & 0 & 1 \end{pmatrix}, \end{aligned} \tag{2.9}$$

where we have used the shorthand notation $c_{ij}^{\theta} = \cos\theta_{ij}$ and $s_{ij}^{\theta} = \sin\theta_{ij}$. The matrix O is parametrised as

$$\begin{aligned} O &= O_{23}\, O_{13}\, O_{12} \\ &= \begin{pmatrix} 1 & 0 & 0 \\ 0 & c_{23}^{\phi} & s_{23}^{\phi} \\ 0 & -s_{23}^{\phi} & c_{23}^{\phi} \end{pmatrix} \begin{pmatrix} c_{13}^{\phi} & 0 & s_{13}^{\phi} \\ 0 & 1 & 0 \\ -s_{13}^{\phi} & 0 & c_{13}^{\phi} \end{pmatrix} \begin{pmatrix} c_{12}^{\phi} & s_{12}^{\phi} & 0 \\ -s_{12}^{\phi} & c_{12}^{\phi} & 0 \\ 0 & 0 & 1 \end{pmatrix}, \end{aligned} \tag{2.10}$$

with $c_{ij}^{\phi} = \cos\phi_{ij}$ and $s_{ij}^{\phi} = \sin\phi_{ij}$, and the diagonal matrices D and d are parametrised as

$$D = \mathrm{diag}(D_1, D_2, D_3) \qquad \text{and} \qquad d = \mathrm{diag}(e^{i\gamma_1}, e^{i\gamma_2}, e^{i\gamma_3})\,. \tag{2.11}$$

In total the coupling matrix λ then has the following 15 physical parameters:

$$\theta_{23},\, \theta_{13},\, \theta_{12},\, \phi_{23},\, \phi_{13},\, \phi_{12},\, \delta_{23},\, \delta_{13},\, \delta_{12},\, \gamma_1,\, \gamma_2,\, \gamma_3,\, D_1,\, D_2,\, D_3\,. \tag{2.12}$$

In order to avoid a double-counting of the parameter space in our numerical analysis, we restrict the parameters of the coupling matrix λ to the following ranges:

$$\theta_{ij} \in [0, \frac{\pi}{4}], \quad \phi_{ij} \in [0, \frac{\pi}{4}], \quad \delta_{ij} \in [0, 2\pi), \quad \gamma_i \in [0, 2\pi), \quad D_i > 0\,. \tag{2.13}$$

2.3 Mass Spectrum and Dark Matter Stability

Following the DMFV assumption the mass term M_χ cannot be a generic 3×3 matrix, as this would constitute an additional source of flavour violation. Instead, similarly to the MFV spurion expansion [12], we can expand the DM mass matrix in powers of the flavour violating coupling λ:

$$M_{\chi,ij} = m_\chi \left\{ \mathbb{1} + \frac{\eta}{2} \left(\lambda^\dagger \lambda + \lambda^T \lambda^*\right) + \mathcal{O}(\lambda^4) \right\}_{ij}\,. \tag{2.14}$$

The expansion parameter η is an additional parameter of the simplified model that accounts for our ignorance of the UV completion of the theory. In order to ensure that the mass corrections always reduce the DM mass with respect to the leading-order mass parameter m_χ, we choose $\eta < 0$.

The expression in eq. (2.14) differs from the one employed in the case of Dirac DM [17] – the second summand in the round brackets is required in order to render the mass matrix symmetric, as required for Majorana fermions. Inserting our parametrization for λ we find

$$M_{\chi,ij} = m_\chi \left\{ \mathbb{1} - \frac{|\eta|}{2} \left(d^*\, O^T\, D^2\, O\, d + d\, O^T\, D^2\, O\, d^*\right) + \mathcal{O}(\lambda^4) \right\}_{ij}\,. \tag{2.15}$$

Note that in contrast to the Dirac fermion case the mass matrix M_χ is not diagonal per se, i.e. there is a misalignment between the flavour and the mass eigenstates for χ. The diagonalization of M_χ can be achieved through an Autonne-Takagi factorization [26, 27], where

$$M_\chi = W^T M_\chi^D W \,. \tag{2.16}$$

Here, M_χ^D is a diagonal matrix with real positive entries and W is an orthogonal matrix, since the mass matrix M_χ is real. The necessary field redefinition $\chi_L \to W\chi_L$ then transforms the coupling of the DM field χ to the SM quarks u_R to

$$\tilde{\lambda} = \lambda W^T \,. \tag{2.17}$$

We further arrange the rows of W in such a way that we always have

$$M_\chi^D = \mathrm{diag}(m_{\chi_1}, m_{\chi_2}, m_{\chi_3}) \,, \tag{2.18}$$

with $m_{\chi_1} > m_{\chi_2} > m_{\chi_3}$, i. e. the third dark generation is the lightest state, and we assume it to form the DM of the universe. Due to the complexity of the mass corrections it is not possible to provide an analytical expression for W and thus, calculating analytical conditions that the model parameters have to fulfil in order to generate a particular mass splitting, as was done in [17], is not possible.

In DMFV models with Dirac fermions DM stability is guaranteed by an unbroken $\mathbb{Z}_3$ symmetry which follows from the flavour symmetry [16, 17, 19][1]. However, for Majorana DM this symmetry cannot be present due to its non-trivial representation being complex. Hence, we impose a $\mathbb{Z}_2$ symmetry under which only the new particles χ and ϕ are charged in order to forbid the decay of χ and ϕ into final states with SM particles only. The lightest flavour of the DM triplet χ is then rendered stable, as long as its mass is smaller than the mass of the coloured scalar boson ϕ. Thus, we additionally choose

$$m_\chi < m_\phi \,. \tag{2.19}$$

3 Collider Phenomenology

Searches for new particles at the LHC lead to stringent constraints on the model presented above. We discuss these constraints in this section to determine the experimentally excluded regions in the parameter space of our model.

It was shown in [28] that for models with a coloured t-channel mediator the most stringent limits arise in general from the pair-production of the mediator, subsequently decaying into quarks and missing transverse energy ($\not{E}_T$), as opposed to searches for monojet+$\not{E}_T$. The authors of [16] found very similar results for a DMFV model where χ is a Dirac fermion and couples to right-handed down-type quarks. We expect that this behaviour also applies to our model and therefore focus on ϕ pair production.

The relevant final states constrained by the LHC experiments are those of searches for supersymmetric top squarks ($t\bar{t} + \not{E}_T$) and squarks of the first two generations (jets+$\not{E}_T$). Note that the limits used in [17] to constrain the Dirac version of top-flavoured DM were based on LHC run 1 data with $\sqrt{s} = 8\,\mathrm{TeV}$. Updated bounds resulting from a recast of

[1] An analogous residual symmetry had previously been found in the case of DM models with MFV [4].

$136\,\text{fb}^{-1}$ of LHC run 2 data at $\sqrt{s} = 13\,\text{TeV}$ were presented in [23]. In this study we will use the same run 2 limits as in [23] to constrain our model of flavoured Majorana DM.

3.1 LHC Signatures from Mediator Pair-Production

Just like squarks in SUSY, the scalar boson ϕ is a colour triplet that is odd under a $\mathbb{Z}_2$ symmetry and is therefore produced in pairs through QCD interactions. Note that this production channel neither depends on the DM mass m_χ nor on the coupling λ.

However, ϕ can also be pair-produced through processes involving the t-channel exchange of χ, as shown in Figure 3.1. These diagrams are proportional to λ^2. As χ is a Majorana fermion the production modes for ϕ also include same-sign production channels, i.e. the mediator can be produced as $\phi\phi^\dagger, \phi\phi$ and $\phi^\dagger\phi^\dagger$ pairs. Note the production of a $\phi\phi$ pair is enhanced by the up quark parton distribution function (PDF) [29], due to the pair of valence up quarks in the proton. As it is the mass term of eq. (2.5) that mixes $\chi_L^\dagger$ and χ_L, these production channels are additionally proportional to the mass parameter m_χ of the Lagrangian.

Due to the $\mathbb{Z}_2$ symmetry introduced in section 2.3 the scalar boson ϕ can only decay into final states that include χ. The by far dominant decay modes are then the ones into a single quark q_i accompanied by χ_j, where i, j are flavour indices, as depicted in Figure 3.2.

Combining the pair-production and decay of the mediator boson ϕ, we find the following parton level processes that are relevant for the LHC analysis:

$$\begin{aligned} pp &\to \phi\,\phi^\dagger \to \chi_i\,\chi_j\,q_k\,\bar{q}_l\,, \\ pp &\to \phi\,\phi \to \chi_i\,\chi_j\,q_k\,q_l\,, \\ pp &\to \phi^\dagger\,\phi^\dagger \to \chi_i\,\chi_j\,\bar{q}_k\,\bar{q}_l\,. \end{aligned} \tag{3.1}$$

Here, i, j, k and l are flavour indices. The explicit constellation of the final states at the LHC depends on the SM flavour indices k and l. An (anti)quark of the first or second generation leads to a jet in the final state which is very difficult to distinguish in flavour. Top and anti-top quarks, however, can be experimentally distinguished in their semileptonic decay channels, by measuring the charge of the final-state lepton. The dark flavours χ_i, on the other hand, are indistinguishable at the LHC, as they appear as missing transverse energy $\not{E}_T$ – due to the small mass splitting possible decay products of the heavy flavours are too soft to be detected.

The relevant final state signatures for the processes discussed above are then $t\bar{t}+\not{E}_T$, $tt+\not{E}_T$, $\bar{t}\bar{t}+\not{E}_T$, and $jj+\not{E}_T$. The former three are not distinguished experimentally if hadronically decaying top quarks are considered. In that case we use the shorthand notation tops $+\not{E}_T$ for the sum of these three processes. The signatures tops $+\not{E}_T$ and $jj+\not{E}_T$ are the same as in SUSY searches for a pair of squarks decaying into SM quarks and a neutralino. As the

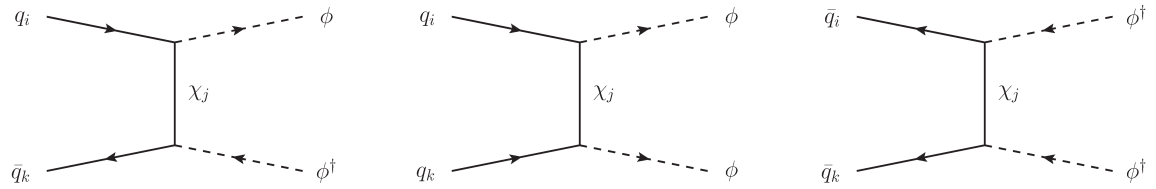

(a) $\phi\phi^\dagger$ production **(b)** $\phi\phi$ production **(c)** $\phi^\dagger\phi^\dagger$ production

Figure 3.1: Feynman diagrams of the t-channel χ exchange production modes of ϕ.

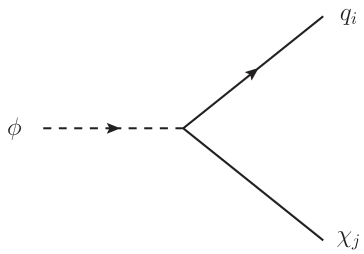

Figure 3.2: Feynman diagram of the mediator decay.

spin-statistics in the SUSY case and in our model are the same, the final-state kinematics is the same as far as the QCD production channel is concerned. For the t-channel production specific to our model, the final-state kinematics could be different, however we do not expect a relevant impact on our results. Thus, we can straightforwardly transfer the limits obtained by such SUSY searches to our case.

It is also possible that the two intermediate ϕ bosons decay into two χ particles, one top quark and one light quark, generating the signature $tj + \not{E}_T$, which is also generated in SUSY models with flavour violating squark decays [21, 30–34]. While no dedicated searches for this signature currently exist, it has been shown in [23] to have significant discovery potential in the case of Dirac DM. We expect that similar conclusions also hold in our model, but leave a detailed analysis for future work.

Lastly, the enhanced same-sign signature $tt + \not{E}_T$ is a unique feature of Majorana DM models which, to the best of our knowledge, has not received attention in the literature. We return to this signature in Section 3.3.

3.2 Recast of LHC Constraints

For the analysis of constraints that LHC searches for SUSY squarks pose on our model, we use the bounds obtained by the CMS collaboration [35] using the full run 2 data set with an integrated luminosity of $136\,\mathrm{fb}^{-1}$. Their analysis places limits on coloured SUSY particles from final states with multiple hadronic jets associated by $\not{E}_T$. In particular, the final states of interest $jj + \not{E}_T$ and tops $+ \not{E}_T$ are directly addressed in that analysis, and cross-section limits are provided in tabular form. Note that the results of [35] are not distinctive with respect to the charge of the final state top quarks.

In order to recast the experimental limits we calculate the leading order (LO) signal cross-section using `MadGraph 5` [36]. The simplified model is implemented in `FeynRules` [37] using the Lagrangian in eq. (2.2). Note that for simplicity we assume a degenerate mass spectrum for the DM triplet χ and neglect the small mass splitting that was discussed in Section 2.3. This approximation is justified as the mass splitting would only lead to additional soft decay products that are difficult to detect and therefore do not qualitatively influence the results of this analysis [17]. As we are primarily interested in the constraints that the LHC searches impose on the mass parameters m_ϕ and m_χ, we set the mixing angles and phases in the coupling matrix λ to zero. Non-zero mixing angles tend to reduce the branching ratio of a given flavour-conserving final state in comparison to the case with vanishing mixing angles, and therefore lead to a smaller signal cross-section. We also assume $D_1 = D_2$ for simplicity.

In Figure 3.3 we show the exclusion contours resulting from the final state tops $+ \not{E}_T$ in the

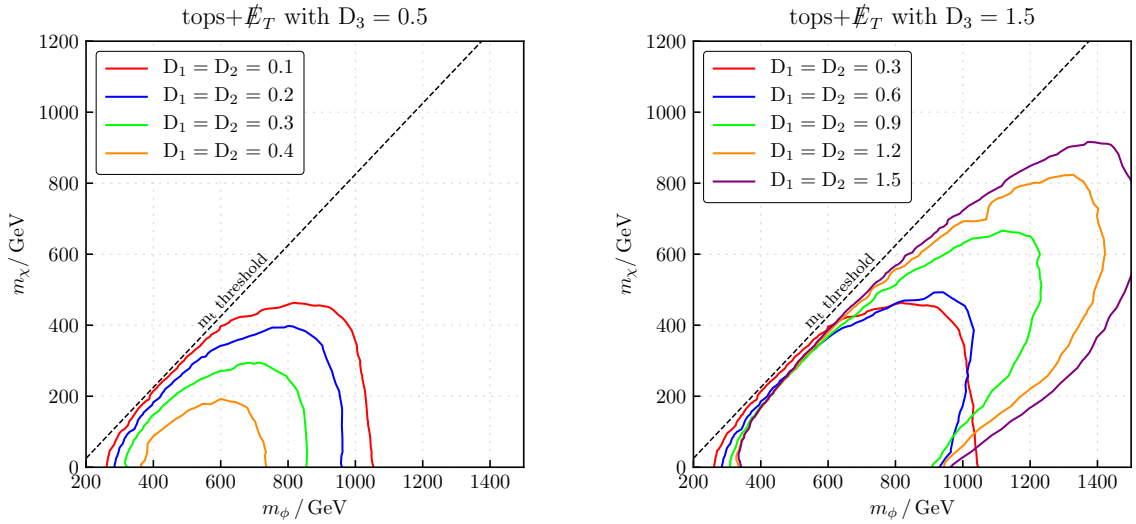

(a) $D_3 = 0.5$ and varying $D_1 = D_2$

(b) $D_3 = 1.5$ and varying $D_1 = D_2$

Figure 3.3: Constraints on the final states $t\bar{t} + \not{E}_T$, $tt + \not{E}_T$ and $\overline{t}\overline{t} + \not{E}_T$ obtained from [35]. The area under the curve is excluded.

$m_\phi - m_\chi$ plane, obtained by recasting the cross-section limits of [35]. The value of D_3 is fixed whereas $D_1 = D_2$ is varied. In Figure 3.3a the excluded region shrinks with growing couplings $D_1 = D_2$. This is due to the fact that increasing the couplings to up and charm quarks reduces the branching ratio of the mediator ϕ decaying into final states with top flavour.

At the same time a growing coupling D_1 enhances the t-channel production process. In Figure 3.3b one can see that due to this reason for couplings $D_1 > 0.5$ the excluded area grows for increasing values of $D_1 = D_2$. Note that in this case contributions of the t-channel production of ϕ proportional to λ^2 grow larger than the QCD contributions to the overall cross-section. In particular, a large coupling D_1 also enhances the production of the same sign final state $tt + \not{E}_T$, enhanced by the PDFs of two up quarks in the initial state. This can be seen explicitly in Figure 3.3b. The excluded region grows quickly for increasing D_1 and non-vanishing DM mass m_χ. As explained above, this dependence on m_χ originates from the Majorana nature of χ necessary for this contribution. Thus, even for the maximally constraining case of $D_1 = D_2 = D_3 = 1.5$ regions with a small m_χ and $m_\phi \gtrsim 1\,\text{TeV}$ are not excluded.

The results of recasting the $jj + \not{E}_T$ limits are shown in Figure 3.4. In this case we fix the value of $D_1 = D_2$ and vary the value of D_3. In contrast to the final states with top flavour, increasing the value of D_3 reduces the branching ratio into this final state. At the same time, both the mediator pair-production cross-section and the final state branching ratio grow with increasing $D_1 = D_2$. The pattern in Figure 3.4 matches this expectation. We observe that an increasing value of D_3 shrinks the excluded area. When comparing Figure 3.4a and Figure 3.4b, we also see that the excluded region grows sizeably when the values of D_1 and D_2 are increased. While this in general is due to an increased production cross-section and branching ratio, it partially originates – in analogy to the final states with top flavour – from the production rate of the same-sign intermediate $\phi\phi$ state that grows for an increasing

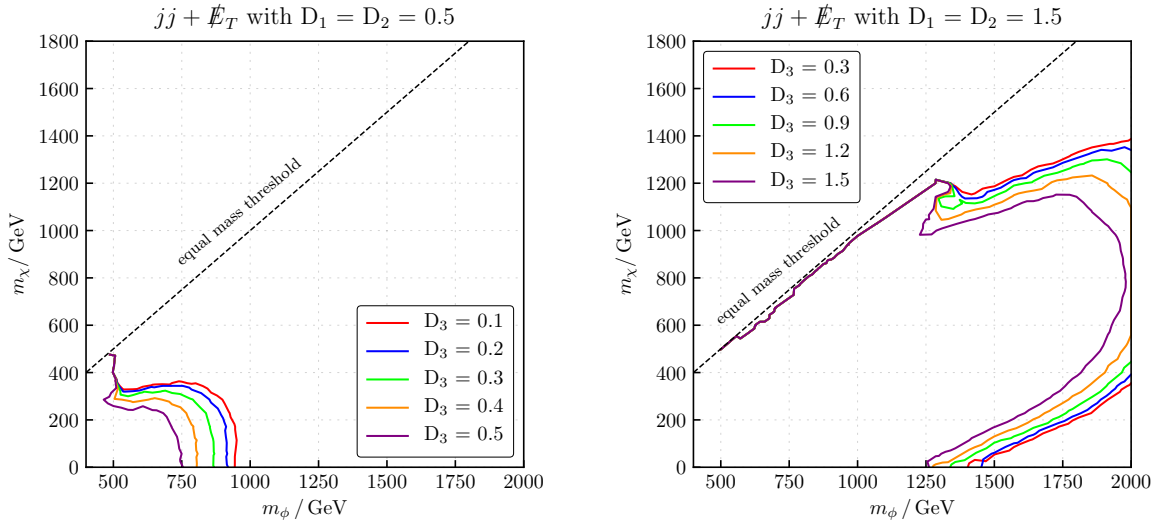

(a) $D_1 = D_2 = 0.5$ and varying D_3

(b) $D_1 = D_2 = 1.5$ and varying D_3

Figure 3.4: Constraints on the final state $jj + \not{E}_T$ obtained from [35].

value of D_1 and is again governed by the mass parameter m_χ. Just as for the final states with top flavour, regions with a small m_χ are therefore not excluded for sufficiently high mediator masses $m_\phi \gtrsim 1.5\,\text{TeV}$. Overall, comparing Figure 3.3 and Figure 3.4 shows that the limits for final states with two jets are significantly more constraining for large $D_1 = D_2$ than the limits for final states with top flavour. As there is no interplay between a decreased branching ratio into the final state and a concurrent increased production of the intermediate state when increasing the value of D_1, this was to be expected. Another reason is that for degenerate couplings D_i the branching ratio of the final state with $jj + \not{E}_T$ is larger, due to the larger multiplicity of possible parton-level final states (u- and c-jets).

In total, we conclude that for both signatures the same-sign contributions present only in the Majorana DM model constrain a significant part of the $m_\phi - m_\chi$ plane. In order to avoid large exclusion limits on the masses, we require D_1 and D_2 to be small. As this choice ensures the t-channel production of ϕ to be small compared to its QCD production, it is safe for D_3 to have larger values. Requiring the couplings to lie in the ranges

$$\begin{aligned} 0 < D_3 \leq 1.5\,, \\ 0 < D_1, D_2 \leq 0.5\,, \end{aligned} \tag{3.2}$$

it is possible to fulfil the LHC constraints for masses $m_\phi \gtrsim 1\,\text{TeV}$ and arbitrary m_χ. As we will see later on, the limits from flavour and DM phenomenology support this choice of ranges especially in the case of top-flavoured DM. Note that even for larger values $D_1, D_2 \gtrsim 1.0$ it is still possible to fulfil the LHC constraints by choosing $m_\phi \gtrsim 1.5\,\text{TeV}$ and $m_\chi \lesssim 200\,\text{GeV}$.

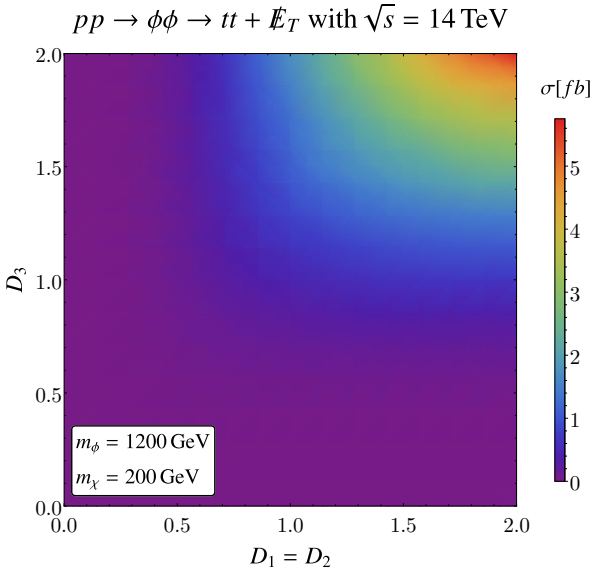

Figure 3.5: LO cross section of $pp \to \phi\phi \to tt + \not{E}_T$ in 14 TeV collisions for $m_\phi = 1200\,\text{GeV}$ and $m_\chi = 200\,\text{GeV}$.

3.3 Same-sign tops at the LHC

As discussed above, the t-channel exchange of a Majorana fermion χ leads to the production of same-sign mediator pairs $\phi\phi$, with the cross-section being enhanced by two powers of the up quark PDF of the proton. The subsequent decay of both ϕ scalars into a top quark and a DM flavour then induces the same-sign di-top final state $tt + \not{E}_T$. Since this signature is absent in the case of Dirac DM and strongly suppressed by the smallness of the relevant couplings in SUSY, we regard this final state as a smoking-gun signature of our model. Experimentally, this final state can be distinguished from the more common $t\bar{t} + \not{E}_T$ one by measuring the lepton charge of semileptonic top decays.

Therefore we also present a prediction for the $tt + \not{E}_T$ production cross section for the upcoming LHC runs, i.e. at a centre of mass energy of $\sqrt{s} = 14\,\text{TeV}$. Note that experimental NP searches dedicated to same-sign top signatures exist, see [38]. The limits obtained in the latter study generally also pose constraints on our model. However, the NP processes under consideration are different from our case, and hence the final-state kinematics are not the same. A proper recasting would therefore be in order to derive meaningful bounds on the parameter space of our model, which is beyond the scope of the present paper.

Figure 3.5 illustrates the LO cross-section for the same-sign signature $tt + \not{E}_T$ for a centre-of-mass energy of $\sqrt{s} = 14\,\text{TeV}$. The cross-section is calculated for varying coupling strengths $D_1 = D_2$ as well as D_3, whereas the masses are fixed to $m_\phi = 1200\,\text{GeV}$ and $m_\chi = 200\,\text{GeV}$, in agreement with the LHC constraints derived in the previous section. As expected, the cross-section grows with an increasing coupling D_1 since the same-sign intermediate state is mainly produced through the process $uu \to \phi\phi$. At the same time, the branching ratio into top final states grows for increasing D_3, yielding the largest $tt + \not{E}_T$ in the part of the parameter space where all couplings D_i are large. In this case, rates of the order of several fb are predicted, well in the reach of future LHC studies.

4 Flavour Physics Phenomenology

A central aspect of the DMFV ansatz is the introduction of the new flavour and CP-violating coupling λ which can generally lead to large FCNC effects and therefore is very sensitive to constraints stemming from flavour observables. Often, the most stringent constraints on flavoured NP interactions stem from $\Delta F = 2$ observables, i. e. observables measuring the oscillation of neutral mesons. Since in our model the new particles couple to the right-handed up-type quarks, the relevant process is $D^0 - \bar{D}^0$ mixing ($\Delta C = 2$), to which we dedicate this section. We derive the relevant expressions for the contributions of our flavoured Majorana DM model and restrict the structure of the coupling matrix λ through existing experimental bounds on $D^0 - \bar{D}^0$ mixing observables. A detailed introduction into the underlying formalism of effective Hamiltonians describing flavour violating processes can be found in [39, 40].

Concerning $\Delta F = 1$ processes, the constraints on NP contributions to rare D decays are generally weaker than the ones from $D^0 - \bar{D}^0$ mixing, and we do not consider them here. Following [17] we also ignore rare flavour violating top decays, as their constraints are not stringent enough yet. However, after combining all available constraints on the parameter space of our model, in Section 8 we return to flavour physics and study the contributions to directly CP-violating charm decays, measured in the asymmetry $\Delta A_{CP}^{\text{dir}}$.

4.1 Neutral D Meson Mixing

The flavour violating interaction term in eq. (2.2) gives rise to NP contributions to $D^0 - \bar{D}^0$ mixing. This $\Delta C = 2$ process is first generated at one-loop order, i.e. $\mathcal{O}(\lambda^4)$. The relevant diagrams are shown in Figure 4.1. Note that the crossed diagram shown in Figure 4.1b only exists if χ is a Majorana fermion. In models where χ is a Dirac fermion one only has the standard box diagram shown in Figure 4.1a. Using the techniques presented in [39, 40] and evaluating the diagrams one arrives at the following effective Hamiltonian:

$$\mathcal{H}_{\text{eff}}^{\Delta C=2,\,\text{NP}} = \frac{1}{128\pi^2 m_\phi^2} \sum_{ij} \lambda_{uj}\lambda_{ci}^* \Big[\lambda_{ui}\lambda_{cj}^* \cdot F(x_i, x_j) - 2\lambda_{uj}\lambda_{ci}^* \cdot G(x_i, x_j)\Big] \times Q_{uc}^{VRR} + h.c.\,, \quad (4.1)$$

where we have used the short-hand notation

$$Q_{uc}^{VRR} = (\bar{u}_\alpha \gamma_\mu P_R c_\alpha)(\bar{u}_\beta \gamma_\nu P_R c_\beta) \quad (4.2)$$

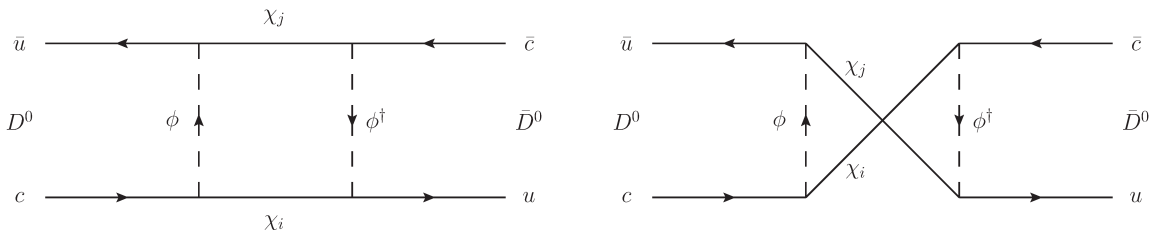

(a) standard box diagram **(b)** crossed box diagram

Figure 4.1: Feynman diagrams for the NP contributions to $D^0 - \bar{D}^0$ mixing at LO.

for the relevant effective four-fermion operator. The loop functions read

$$F(x_i, x_j) = \left(\frac{x_i^2 \log(x_i)}{(x_i - x_j)(1 - x_i)^2} + \frac{x_j^2 \log(x_j)}{(x_j - x_i)(1 - x_j)^2} + \frac{1}{(1 - x_i)(1 - x_j)} \right),$$
$$G(x_i, x_j) = -\left(\frac{\sqrt{x_i x_j} x_i \log(x_i)}{(x_i - x_j)(1 - x_i)^2} + \frac{\sqrt{x_i x_j} x_j \log(x_j)}{(x_j - x_i)(1 - x_j)^2} + \frac{\sqrt{x_i x_j}}{(1 - x_i)(1 - x_j)} \right), \tag{4.3}$$

with $x_i = m_{\chi_i}^2 / m_\phi^2$. In eq. (4.2) we imply a summation over the colour indices α and β. In the interval $x_i \in [0, 1]$ the loop functions of eq. (4.3) have the same sign, i.e. the two diagrams of Figure 4.1 can interfere destructively due to the relative minus sign in the effective Hamiltonian in eq. (4.1). This is a well known effect from SUSY where the box diagram contains a squark and a gluino [41]. For $x_i = x_j = 1$ we even have $2G(1, 1) = F(1, 1)$, but as the coupling λ is not flavour-universal a destructive interference can only occur in eq. (4.1) if the different prefactors of $F(x_i, x_j)$ and $G(x_i, x_j)$ have the same sign.

Using the effective Hamiltonian from above we can now calculate the off-diagonal element of the $D^0 - \bar{D}^0$ mass matrix as

$$\begin{aligned} M_{12}^{D,\,\mathrm{NP}} &= \frac{1}{2m_D} \langle \bar{D}^0 | \, \mathcal{H}_{\mathrm{eff}}^{\Delta C=2,\,\mathrm{NP}} \, | D^0 \rangle^* \\ &= \frac{\eta_D m_D f_D^2 \hat{B}_D}{384\pi^2 m_\phi^2} \sum_{ij} \lambda_{uj}^* \lambda_{ci} \Big[\lambda_{ui}^* \lambda_{cj} \cdot F(x_i, x_j) - 2\lambda_{uj}^* \lambda_{ci} \cdot G(x_i, x_j) \Big], \end{aligned} \tag{4.4}$$

where we have used

$$\langle \bar{D}^0 | \, Q_{uc}^{VRR}(\mu) \, | D^0 \rangle = \frac{2}{3} m_D^2 f_D^2 \hat{B}_D \tag{4.5}$$

for the hadronic matrix element at the meson scale $\mu = 3\,\mathrm{GeV}$. The parameters f_D and $\hat{B}_D$ are obtained through lattice QCD calculations at this scale [42, 43]. In eq. (4.4) the parameter η_D accounts for NLO contributions from the renormalization group running between the weak scale $\mu = M_W$ and the D^0 meson scale $\mu = 3\,\mathrm{GeV}$ [44]. It also serves as a parametrisation of threshold corrections for the matching of the SM to the effective theory. We neglect the additional threshold matching corrections between the SM and our DMFV model which, following [16], we expect to be small. Also note that there is no NP contribution to the absorptive part of the mixing amplitude Γ_{12}^D, since the NP scale is above the D^0 meson mass scale and therefore cannot contribute on-shell.

The expression in eq. (4.4) describes the general case with a possible mass splitting between different DM flavours χ_i. As the mass corrections described in Section 2.3 are NLO in the DMFV expansion, plugging them into the expressions from above will generate a higher-order DMFV correction that we assume to be small. Further, we have checked numerically that $x_i \neq x_j$ only causes corrections of a few percent for the loop functions $F(x_i, x_j)$ and $G(x_i, x_j)$. Thus, the mass splitting among the fields χ_i is neglected in this section. We can then evaluate the sum in eq. (4.4) and find

$$M_{12}^{D,\,\mathrm{NP}} = \frac{\eta_D m_D f_D^2 \hat{B}_D}{384\pi^2 m_\phi^2} \Big[\xi_f \cdot f(x) - 2\,\xi_g \cdot g(x) \Big], \tag{4.6}$$

where we have introduced

$$\xi_f = \sum_{ij} \lambda^*_{ui}\lambda_{ci}\lambda^*_{uj}\lambda_{cj} = \left(\lambda\lambda^\dagger\right)^2_{cu} ,$$
$$\xi_g = \sum_{ij} \lambda_{ci}\lambda_{ci}\lambda^*_{uj}\lambda^*_{uj} = \left(\lambda\lambda^T\right)_{cc}\left(\lambda\lambda^T\right)^*_{uu} . \tag{4.7}$$

For the loop functions we find

$$f(x) = \lim_{y\to x} F(x,y) = \frac{1+x}{(1-x)^2} + \frac{2x\log(x)}{(1-x)^3} , \tag{4.8}$$
$$g(x) = \lim_{y\to x} G(x,y) = -\frac{2x}{(1-x)^2} - \frac{x(1+x)}{(1-x)^3}\log(x) . \tag{4.9}$$

We can now calculate the NP contribution to x_{12}^D according to

$$x_{12}^{D,\mathrm{NP}} = 2\,\tau_{D^0}\,|M_{12}^{D,\mathrm{NP}}| . \tag{4.10}$$

As $\Gamma_{12}^{D,\mathrm{SM}}$ is real to an excellent approximation in the standard parametrisation of the CKM matrix, the CP-violating phase simply reduces to $\phi_{12}^D = \mathrm{Arg}\left(M_{12}^D\right)$.

4.2 Application of the D meson mixing constraints

In Table 4.1 we show the relevant values of parameters and the model-independent limits for x_{12}^D as well as ϕ_{12}^D that we use in the numerical analysis.

For a proper treatment of the restrictions these constraints pose on λ it is necessary to also consider the SM contribution to x_{12}^D and ϕ_{12}^D. As the CP-violating phase is expected to be of order $\mathcal{O}(10^{-3})$ in the SM, we neglect this small contribution and assume $M_{12}^{D,\mathrm{SM}}$ to be real. As for the SM contributions to x_{12}^D, they are dominated by long-distance effects and hence suffer from large theory uncertainties. Nevertheless, estimates of $x_{12}^{D,\mathrm{SM}}$ find it of the order $\mathcal{O}(10^{-2})$ [47]. Given these uncertainties, we conservatively assume the SM contribution to lie

Numerical Values and Limits	
$\hat{B}_D$	0.75 ± 0.02
f_D	$209.0 \pm 2.4\,\mathrm{MeV}$
η_D	0.772
m_{D^0}	$1864.83 \pm 0.05\,\mathrm{MeV}$
τ_{D^0}	$410.1 \pm 1.5\,\mathrm{fs}$
x_{12}^D	$[0.21\%, 0.63\%]$
ϕ_{12}^D	$[-2.8^\circ, 1.7^\circ]$

Table 4.1: Numerical values and limits used for the analysis of the $D^0 - \bar{D}^0$ mixing constraints [42–46]. The limits on x_{12}^D and ϕ_{12}^D are given at 95% C.L. and were obtained from the Heavy Flavour Averaging Group's (HFLAV) website [46].

in the range

$$x_{12}^{D,\mathrm{SM}} \in [-3\%, 3\%]\,. \tag{4.11}$$

Using the results provided in the previous section we then demand that the total values for x_{12}^D and ϕ_{12}^D lie in their 95% C.L. intervals given in Table 4.1 to restrict the parameters of our model. The results are shown in Figure 4.2, Figure 4.3 and Figure 4.4.

Figure 4.2 illustrates the allowed mixing angles θ_{ij} in dependence of the difference $\Delta_{ij} = |D_i - D_j|$ for $m_\chi < m_\phi$ and $m_\phi = m_\chi$.[2] We see that in both cases the strongest restrictions are placed on θ_{12} and that the experimental constraints become especially effective for large Δ_{ij}. For nearly degenerate couplings $D_i \simeq D_j$ the corresponding angle θ_{ij} can be chosen freely. The reason is that the factor ξ_f defined in eq. (4.9) approaches zero in the limit of degenerate D_i as $\lambda\lambda^\dagger = UD^2U^\dagger$ becomes diagonal. Thus, the contribution of the diagram in Figure 4.1a vanishes. Figure 4.2b shows that choosing $m_\phi = m_\chi$ only slightly loosens the bounds on Δ_{ij}.

As the crossed box diagram in Figure 4.1b is proportional to the diagonal entries of $\lambda\lambda^T$ and its complex conjugate, it does not approach zero for vanishing mixing angles and phases. In order to gain insight on the constraints this places on the parameters of λ, we analyse the $D_i - D_j$ plane of the parameter space. Figure 4.3a shows that the constraints require the couplings D_1 and D_2 to roughly lie in the interval $D_1, D_2 \in [0.0, 0.5]$. This is due to the fact that ξ_g mainly depends on these two couplings. For zero mixing angles and phases it reduces to $\xi_g = D_1^2 D_2^2$. Thus, combinations of a large D_1 with a small D_2 or vice versa are also allowed. In Figure 4.3b we see that there are no such constraints on D_3 and that the latter coupling can be chosen freely. The same pattern can also be observed for other masses m_ϕ and m_χ.

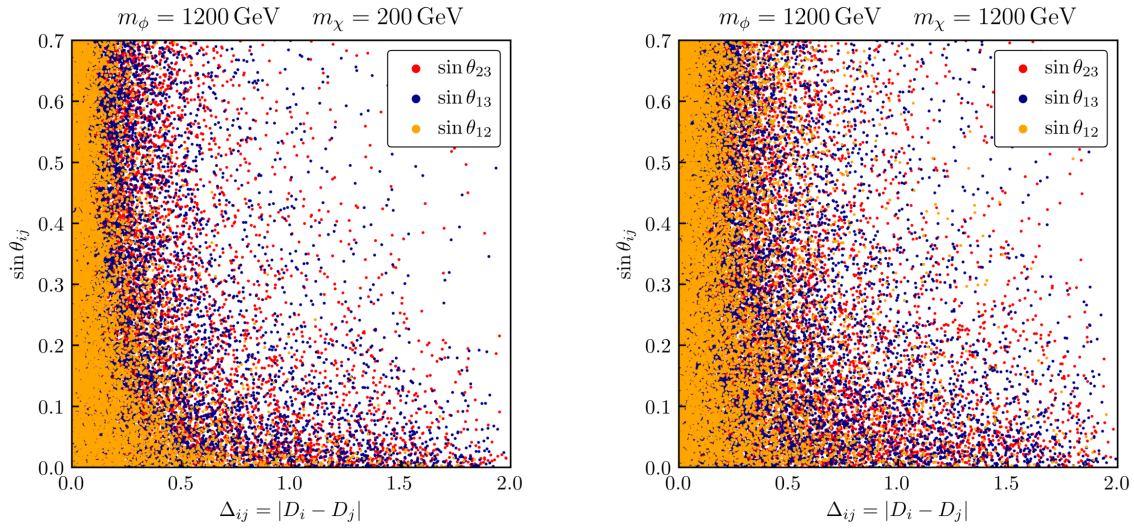

(a) $m_\phi = 1200\,\mathrm{GeV}$ and $m_\chi = 200\,\mathrm{GeV}$ **(b)** $m_\phi = 1200\,\mathrm{GeV}$ and $m_\chi = 1200\,\mathrm{GeV}$

Figure 4.2: Allowed mixing angles θ_{ij} as a function of the splitting $\Delta_{ij} = |D_i - D_j|$ for two choices of m_ϕ and m_χ.

[2] The latter case is excluded as it would render ϕ stable, in conflict with cosmological observations. Nevertheless, we also discuss the case of equal masses here in order to provide a better understanding of the flavour physics phenomenology and the interference between the diagrams shown in 4.1.

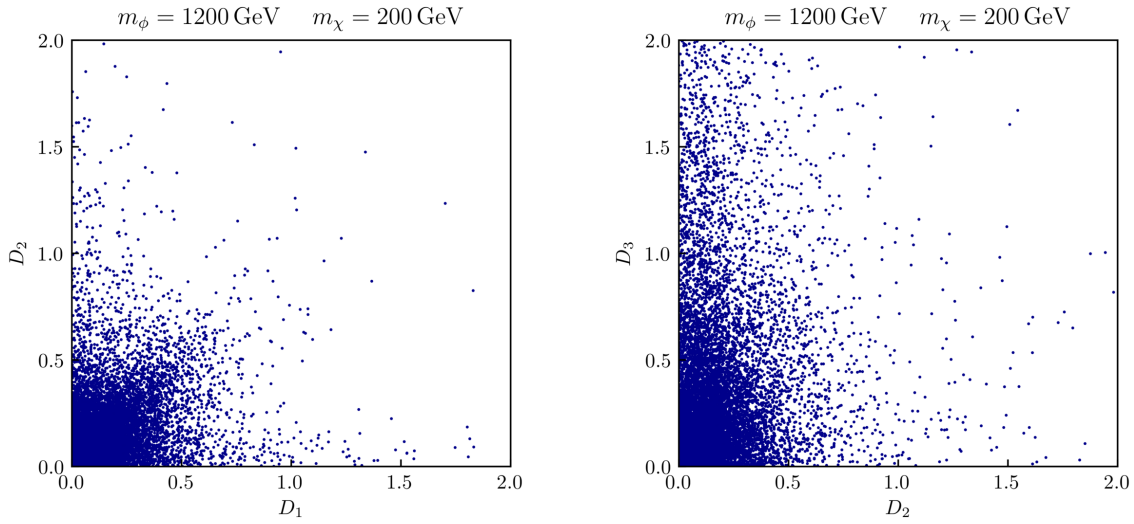

(a) $D_1 - D_2$ plane

(b) $D_2 - D_3$ plane

Figure 4.3: Allowed parameter space in the $D_i - D_j$ plane for $m_\phi = 1200\,\text{GeV}$ and $m_\chi = 200\,\text{GeV}$.

We conclude that, barring fine-tuned cancellations,

$$\begin{aligned} 0 < D_3 \leq 2.0\,, \\ 0 < D_1, D_2 \leq 0.5 \end{aligned} \tag{4.12}$$

is required to fulfil the $D^0 - \bar{D}^0$ mixing constraints while allowing for large mixing angles for most of the remaining parameter space. It is interesting to see that this result perfectly matches the LHC constraints identified in Section 3.2.

As for the aforementioned possible destructive interference of the two diagrams shown in Figure 4.1, we find that the allowed parameter space indeed is mainly determined by it. In Figure 4.4 we show the imaginary parts of ξ_i for two choices for the masses m_ϕ and m_χ to illustrate this effect. One can see that for both choices of masses the allowed imaginary parts scatter around a linear function. Remembering that the limits on ϕ_{12}^D are very stringent, i.e. $\phi_{12}^D \approx 0$, this behaviour can be understood analytically. Since ϕ_{12}^D is given as

$$\phi_{12}^D = \arctan \frac{\text{Im}(M_{12}^{D,\text{NP}})}{\text{Re}(M_{12}^{D,\text{NP}}) + \text{Re}(M_{12}^{D,\text{SM}})} \tag{4.13}$$

small values for ϕ_{12}^D require a small imaginary part of $M_{12}^{D,\text{NP}}$. This requirement forces the two factors ξ_f and ξ_g to follow the relation

$$\text{Im}\xi_f \approx \text{Im}\xi_g \frac{2g(x)}{f(x)}\,. \tag{4.14}$$

We confirm this finding in Figure 4.4a where we have $x = 1$ and $2g(1) = f(1) = 1/3$. In this

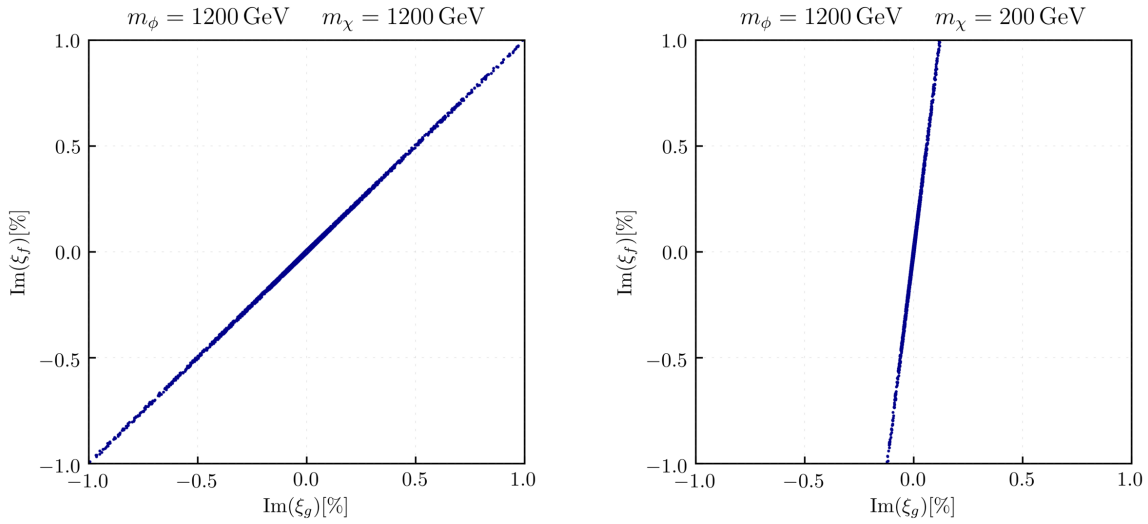

(a) $m_\phi = 1200\,\text{GeV}$ and $m_\chi = 1200\,\text{GeV}$ **(b)** $m_\phi = 1200\,\text{GeV}$ and $m_\chi = 200\,\text{GeV}$

Figure 4.4: Imaginary part of the two factors ξ_f and ξ_g in percent.

case the slope is basically one and we have $\text{Im}\xi_f = \text{Im}\xi_g$. For any other point in the $m_\phi - m_\chi$ plane the slope is given by the actual value of $2g(x)/f(x)$ as can be seen in Figure 4.4b. In the described figures the scattering of the allowed points around this linear function is due to the fact that ϕ_{12}^D is not exactly zero but is allowed to lie in the interval given in Table 4.1. The same interference between the diagrams of Figure 4.1 can also be seen in the real part of $M_{12}^{D,\text{NP}}$, with the sole difference of a larger scattering around the linear function of eq. (4.14). This is due to the theoretical uncertainty in the SM contribution to the real part of M_{12}^D.

5 Cosmological Implications

The constraints from collider and flavour physics experiments analysed so far are generally relevant for any extension of the SM that contains new flavoured particles. As the DMFV ansatz further assumes the lightest flavour of the field χ to constitute the observed DM in the universe [48], it is also necessary to consider constraints from cosmology. Thus, we use this section to discuss the implications of the observed DM relic abundance on our model.

5.1 DM Annihilation and Freeze-Out Scenarios

A commonly used approach to explain the observed amount of DM is to assume a freeze-out of dark particles from thermal equilibrium at a given temperature $T_f \approx m_\chi/20$ [49], i.e. at temperatures below T_f the DM production and annihilation rates both approach zero and one is left with a relic of DM. The resulting relic abundance depends on the annihilation rate of DM into SM matter. We first define two benchmark freeze-out scenarios to be discussed in this analysis and then provide the relevant formulae for the annihilation of DM into SM matter.

As our model contains three generations of DM particles it is important to consider the mass hierarchy of the fields χ_i in order to identify different freeze-out of scenarios. This hierarchy

is generated by the DMFV mass corrections discussed in Section 2.3. If there is only a very small difference between the different DM masses m_{χ_i}, all three flavours will be present at the time of thermal freeze-out since the decay of the slightly heavier flavours into the lightest one is kinematically highly suppressed. The frozen-out heavy flavours will then completely decay into the lightest DM particle at later times or lower temperatures, respectively. If on the other hand we allow for a significant splitting, the heavier DM particles will already have decayed by the time the freeze-out happens. In this case the only flavour that is present at freeze-out is the lightest. We follow [16,17] and define the following two freeze-out scenarios as benchmarks:

- We call the case of a very small mass splitting the **quasi-degenerate freeze-out (QDF)** scenario. In this case the mass difference

$$\Delta m_{i3} = \frac{m_{\chi_i}}{m_{\chi_3}} - 1\,, \tag{5.1}$$

  between the heavier flavours $i \in \{1,2\}$ and the lightest flavour[3] is restricted to be below 1%. In order to suppress the DMFV correction to the DM mass matrix, we set $\eta = -0.01$ in eq. (2.15). Smaller magnitudes of η would be implausible, as the contribution is generated at the one-loop level.

- In the **single flavour freeze-out scenario (SFF)** the mass splitting Δm_{i3} is assumed to be larger than 10% but still small enough to ensure the convergence of eq. (2.15). We choose $\eta = 0.0575$ for this scenario. This yields a maximal splitting of $\Delta m_{i3}^{\max} \simeq 30\%$ for couplings $D_i \leq 2.0$.

The relevant diagram for the DM annihilation process at tree-level is shown in Figure 5.1. Evaluating this diagram we find

$$|\overline{M}|^2 = \frac{1}{9}\cdot\frac{3}{4}\sum_{ij}\sum_{kl}|\tilde{\lambda}_{ki}|^2|\tilde{\lambda}_{lj}|^2\frac{(m_{\chi_i}^2 + m_k^2 - t)(m_{\chi_j}^2 + m_l^2 - t)}{(t - m_\phi^2)^2}\,, \tag{5.2}$$

for the flavour, colour and spin averaged amplitude $\overline{M}$. Here, t is the Mandelstam variable defined as $t = (p_1 - p_3)^2$ and the indices i, j, k and l are flavour indices. Using this result and

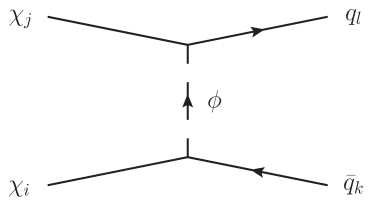

Figure 5.1: Feynman diagram for the annihilation of two DM particles into two SM quarks at LO.

[3] Remember that we conventionally choose the third generation to be the lightest of the three DM particles.

the techniques provided in [50] we find for the effective annihilation cross section

$$\langle\sigma v\rangle_{\text{eff}} = \frac{1}{9}\cdot\frac{3}{512\,\pi\,m_\chi^4}\sum_{ij}\sum_{kl}|\tilde{\lambda}_{ki}|^2|\tilde{\lambda}_{lj}|^2\frac{16\,m_\chi^4-\left(m_{q_k}^2-m_{q_l}^2\right)^2}{\left[m_{q_k}^2+m_{q_l}^2-2\left(m_\chi^2+m_\phi^2\right)\right]^2} \times\sqrt{16\,m_\chi^4+\left(m_{q_k}^2-m_{q_l}^2\right)^2-8\,m_\chi^2\left(m_{q_k}^2+m_{q_l}^2\right)}\,, \tag{5.3}$$

where we have set $m_{\chi_i} = m_{\chi_j} = m_\chi$. For the SFF scenario this step is evident, as only the lightest flavour is present and there is no co-annihilation between different flavours of χ. Note that in this case eq. (5.3) does not contain the flavour averaging factor $1/9$ as there is no sum over the initial state flavours i and j, and the parameter m_χ has to be understood as the mass of the lightest DM particle χ_3. In the QDF scenario, however, all three flavours are present but we demand the mass splittings Δm_{i3} to be smaller than 1%. Thus, setting $m_{\chi_i} = m_{\chi_j}$ is a very good approximation. We have checked that this in fact only causes a negligibly small difference of order $\mathcal{O}(1\%)$ in the results. It is also important to note that the sum over the final state flavours k and l depends on the value of m_χ. If $m_\chi < m_t$, final states with a top anti-top pair are kinematically forbidden. In this case the only allowed final states with top flavour are single-top final states, i.e. the term with $k = l = 3$ is excluded from them sum. For even smaller values with $m_\chi < m_t/2$ final states with top flavour are excluded completely and thus one has $k, l \in \{1, 2\}$. We also state that eq. (5.3) does not contain the additional factor of $1/2$ present in the case of Dirac DM [17] as the DM particles are Majorana fermions in our model [51, 52].

5.2 Analysis of the Relic Abundance Constraints

For the numerical analysis of the relic abundance constraints we demand that

$$\langle\sigma v\rangle_{\text{eff}} = 2.2\cdot10^{-26}\,\text{cm}^3/\text{s}\,, \tag{5.4}$$

within a 10% tolerance range. This value is adopted from [49] and represents the effective annihilation cross section that is necessary to produce the observed relic abundance through a single particle freeze-out for masses $m_\chi > 1\,\text{GeV}$. We further set the masses of the light quarks to zero and use $m_t = 173.5\,\text{GeV}$.

The results are shown in Figure 5.2. The allowed parameter space that we see for the QDF scenario in Figure 5.2a corresponds to the overlap between the allowed parameter space that remains after demanding the QDF mass splitting and after demanding the annihilation cross section to lie in the required range. For masses $m_\chi \gg m_t$ we find

$$\begin{aligned}\langle\sigma v\rangle_{\text{eff}} &= \frac{1}{96\pi}\sum_{ij}\sum_{kl}|\tilde{\lambda}_{ki}|^2|\tilde{\lambda}_{lj}|^2\frac{m_\chi^2}{\left(m_\chi^2+m_\phi^2\right)^2}\\ &= \frac{m_\chi^2}{96\pi\left(m_\chi^2+m_\phi^2\right)^2}\cdot\left(D_1^2+D_2^2+D_3^2\right)^2\,,\end{aligned} \tag{5.5}$$

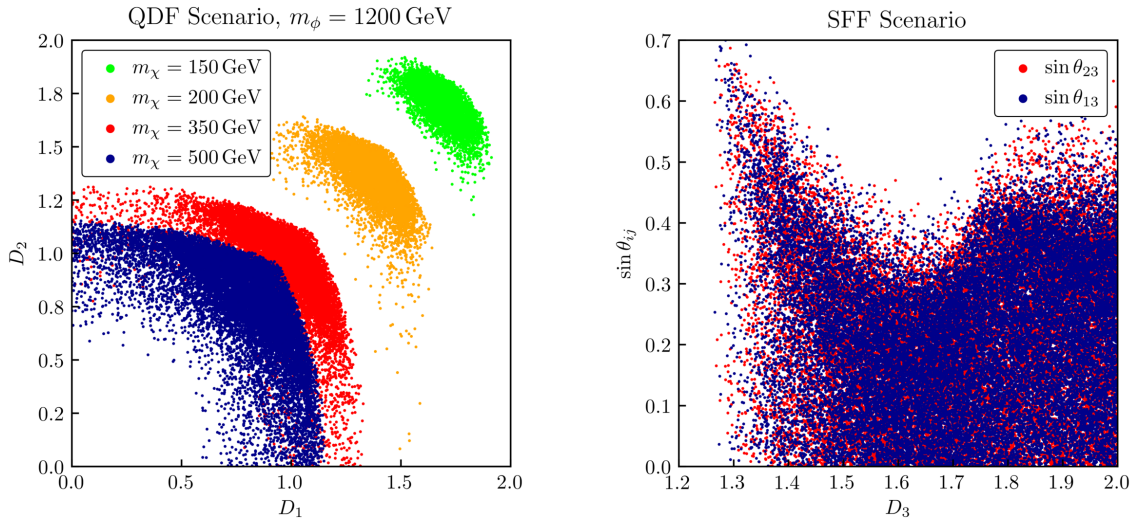

(a) $D_1 - D_2$ plane in the QDF scenario for varying m_χ and $m_\phi = 1200\,\text{GeV}$

(b) Allowed $\sin\theta_{i3}$ and D_3 in the SFF scenario for $m_\chi = 210\,\text{GeV}$ and $m_\phi = 1000\,\text{GeV}$

Figure 5.2: Restrictions of the relic abundance constraints on the model parameters for both freeze-out scenarios.

where we have used

$$\sum_{ij}\sum_{kl}|\tilde{\lambda}_{ki}|^2|\tilde{\lambda}_{lj}|^2 = \text{Tr}\left[\tilde{\lambda}^\dagger\tilde{\lambda}\right]^2 = \text{Tr}\left[W\lambda^\dagger\lambda W^T\right] = \text{Tr}\left[D^2\right]\,. \tag{5.6}$$

Thus, the relic abundance constraint translates into the condition

$$D_1^2 + D_2^2 + D_3^2 \approx \text{const.}\,, \tag{5.7}$$

for a given point in the $m_\phi - m_\chi$ plane. The circular pattern of Figure 5.2a is due to this condition. We recover the same expression for the annihilation cross section in the limit $m_\chi \ll m_t$, as we set the masses of light quarks to zero and final states with top flavour become inaccessible in this limit. The m_χ dependence of $\langle\sigma v\rangle_{\text{eff}}$ can easily be seen, as small masses m_χ require large couplings D_1 and D_2. Another reason for why large couplings are required in the case of small m_χ is the reduced number of annihilation channels due to the exclusion of final states with top flavour for $m_\chi < m_t$ and $m_\chi < m_t/2$ respectively. Given that we restrict the couplings D_i to $D_i \in [0, 2]$ this poses a lower limit on m_χ.

There is no sum over intial state flavours in eq. (5.3) in the SFF scenario as the only flavour contributing to the freeze-out is χ_3. In Figure 5.2b we show the restrictions on the mixing angles θ_{13} and θ_{23} in the SFF scenario for the case of top-flavoured DM, i. e. the lightest flavour χ_3 coupling dominantly to the top quark. We see that for the smallest allowed values of D_3 the mixing angles need to be large, since they parametrize the annihilation of χ_3 into up or charm quarks. In this case the contribution of the annihilation channel into a top-antitop pair alone is not large enough to fulfil the constraint. Large mixing angles lead to additional contributions from annihilations into final states with up or charm quarks and push the overall cross section

into the tolerance interval. Once D_3 is large enough, the constraints on the mixing angles become softer. For even higher values for D_3 we find an upper bound on the mixing angles, as too large values would lead to too large contributions from annihilations into final states with up or charm quarks, pushing the overall annihilation cross-section above the tolerance interval. The upper bound on the mixing angles becomes stronger for values $D_3 \lesssim 1.75$. In the limit of small mixing angles ϕ_{ij} the mass corrections to χ_3 are approximately $m_{\chi_3} \approx m_\chi \left(1 - \eta D_3^2\right)$ and thus final states with a top-antitop pair are kinematically forbidden for values $D_3 \gtrsim 1.75$ as the DM mass m_{χ_3} drops below the top mass threshold. Thus, large mixing angles are allowed here as the contribution of annihilation into light quarks may become larger again. As we do not fix the values of $\sin\theta_{13}$ while looking at $\sin\theta_{23}$ and vice versa, we see no difference for these two mixing angles in Figure 5.2b. Recall that we allow for a rearrangement of the diagonalization matrix W of eq. (2.16) in order to obtain a hierarchy such that the third generation is always the lightest. As this at the same time determines the flavour of χ_3, its mass corrections may also depend on D_1 or D_2 and the respective mixing angles if χ_3 has up or charm flavour. In these cases the parameters shown in Figure 5.2b are basically free, with the only restriction of a sufficiently small D_3 in order to fulfil the SFF mass splitting condition.

Like in the QDF scenario, also in the SFF scenario there is a lower bound on m_{χ_3} due to the upper limit $D_i < 2.0$ we chose in our analysis. Additionally, for the SFF scenario we also find an upper bound on m_{χ_3} as can be seen in Figure 5.3. This upper bound on m_{χ_3} can be explained through eq. (5.3). For large values of m_{χ_3} the couplings $\tilde{\lambda}_{i3}$ have to be correspondingly small in order to keep the annihilation cross section in the allowed interval. At the same time the mass splitting of the SFF scenario forces one $\tilde{\lambda}_{i3}$ to be large. For too large m_{χ_3} it is not possible to maintain the SFF mass splitting while at the same time fulfilling the relic abundance bound and thus, we observe an upper limit. As the mediator mass m_ϕ suppresses the annihilation cross section, the allowed region for m_χ grows with m_ϕ.

In summary, the constraints on our model from the observed relic abundance are very similar to the ones found in the case of Dirac DM [17], the factor of two difference in the effective

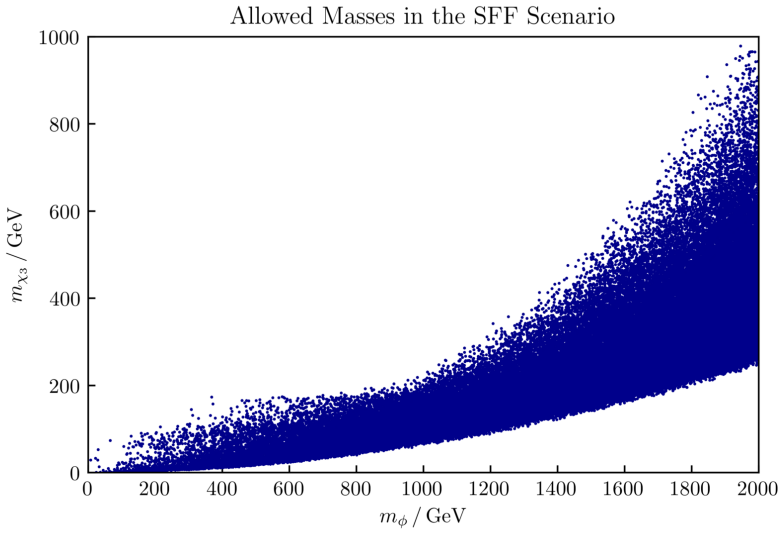

Figure 5.3: Allowed points in the $m_\phi - m_{\chi_3}$ plane for the SFF scenario.

annihilation cross-section, eq. (5.3), plays only a minor quantitative role.

6 Dark Matter Phenomenology

The Majorana nature of the DM field χ has profound implications on its signatures in direct detection experiments. The DM-nucleon scattering cross-section generally splits up into a spin-dependent and spin-independent part in the non-relativistic limit, where constraints on the latter are typically stronger due to a coherent scattering off all nucleons in the nucleus. In the spin-dependent case there is no such enhancement, since the DM particle couples to the modulus of the total spin [53] and the nucleon spins cancel in pairs. Hence, it is sufficient to only consider the spin-independent part of the scattering cross-section, unless it is suppressed, and neglect the spin-dependent contributions [16, 17, 19]. However, for our case of DM with Majorana nature and a chiral coupling the leading dimension-six operators for spin-independent scattering $\bar{\chi}\chi\bar{q}q$ and $(\bar{\chi}\gamma^\mu\chi)(\bar{q}\gamma_\mu q)$ are identically zero due to the coupling structure or since for Majorana particles bilinears which are anti-symmetric under C parity vanish, respectively [53–55]. Thus, it is not only necessary to also include the spin-dependent cross section into the analysis, but also to go beyond leading order and include loop-induced scattering between DM and gluons for the spin-independent part. In Figure 6.1 we show representative Feynman diagrams for the relevant processes.

6.1 DM-Nucleon Scattering Processes

As already mentioned above, the DM-nucleon scattering cross section splits up into a spin-dependent part [54–56]

$$\sigma_{\mathrm{SD}}^N = \frac{3}{16\pi}\frac{m_N^2 m_\chi^2}{(m_N+m_\chi)^2}\left(\sum_{q=u,d,s}\Delta q^N a_q\right)^2 , \tag{6.1}$$

and a spin-independent part [53–55]

$$\sigma_{\mathrm{SI}}^N = \frac{4}{\pi}\frac{m_N^2 m_\chi^2}{(m_N+m_\chi)^2}\,|f_N|^2 , \tag{6.2}$$

where a_q is the Wilson coefficient of the spin-dependent quark-nucleon interaction, Δq^N is the spin content of the nucleon $N=\{p,n\}$ in terms of the quark q and m_N is its mass. The factor f_N is the matrix element of the spin-independent quark-nucleon interaction.

As the NP only couples to up-type quarks in our model, the expression for σ_{SD}^N becomes

$$\sigma_{\mathrm{SD}}^N = \frac{3}{16\pi}\frac{m_N^2 m_\chi^2}{(m_N+m_\chi)^2}\left(\Delta u^N a_u\right)^2 , \tag{6.3}$$

with

$$a_u = \frac{|\tilde{\lambda}_{u3}|^2}{m_\phi^2-(m_\chi+m_u)^2} . \tag{6.4}$$

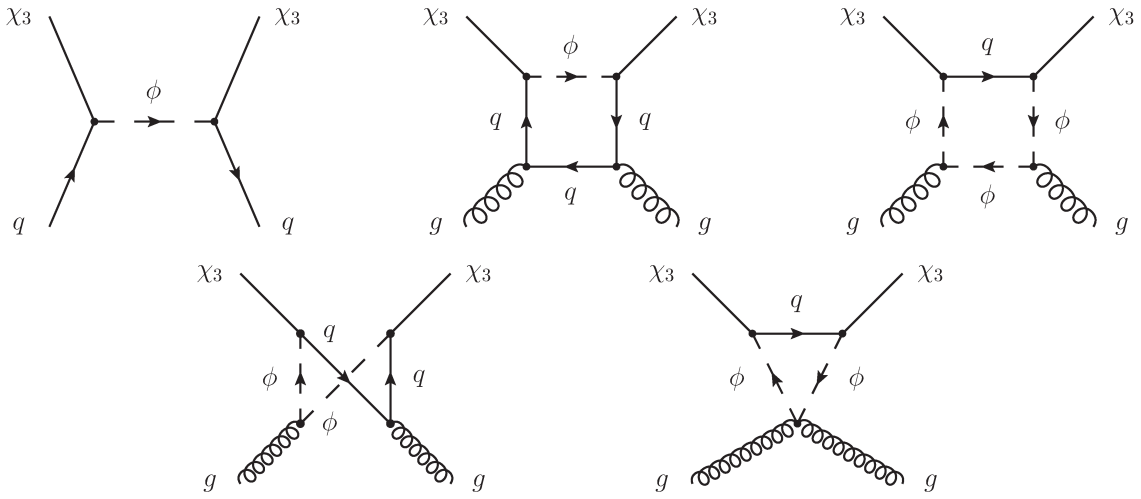

Figure 6.1: Tree-level and loop induced Feynman diagrams for DM-nucleon scattering.

For $\sigma_{\rm SI}$ we follow the formalism of [57, 58] and write the effective interaction Lagrangian as

$$\mathcal{L}_{\rm SI}^{\rm eff} = \sum_{q=u,d,s,c} \mathcal{L}_q^{\rm eff} + \mathcal{L}_g^{\rm eff} \,. \tag{6.5}$$

Here, $\mathcal{L}_q^{\rm eff}$ describes the scattering between DM and quarks, and reads

$$\mathcal{L}_q^{\rm eff} = f_q \bar{\chi}\chi\, \mathcal{O}_q^{(0)} + \frac{g_q^{(1)}}{m_\chi} \bar{\chi} i(\partial^\mu \gamma^\nu + \partial^\nu \gamma^\mu)\chi \mathcal{O}_{q,\mu\nu}^{(2)} + \frac{g_q^{(2)}}{m_\chi^2} \bar{\chi}(i\partial^\mu)(i\partial^\nu)\chi \mathcal{O}_{q,\mu\nu}^{(2)} \,, \tag{6.6}$$

while the loop-induced scattering between gluons and DM is described by

$$\mathcal{L}_g^{\rm eff} = f_G \bar{\chi}\chi\, \mathcal{O}_g^{(0)} + \frac{g_G^{(1)}}{m_\chi} \bar{\chi} i(\partial^\mu \gamma^\nu + \partial^\nu \gamma^\mu)\chi \mathcal{O}_{g,\mu\nu}^{(2)} + \frac{g_G^{(2)}}{m_\chi^2} \bar{\chi}(i\partial^\mu)(i\partial^\nu)\chi \mathcal{O}_{g,\mu\nu}^{(2)} \,. \tag{6.7}$$

Using the notation of [55] the tensor operators can be written as

$$\begin{aligned} \mathcal{O}_{q,\mu\nu}^{(2)} &= \frac{1}{2}\bar{q}\left(\gamma^{\{\mu} i D_-^{\nu\}} - \frac{g^{\mu\nu}}{4} i \not{D}_-\right) , \\ \mathcal{O}_{g,\mu\nu}^{(2)} &= -G^{a,\mu\rho} G^{a,\nu}{}_{\rho} + \frac{g^{\mu\nu}}{4}\left(G^a_{\alpha\beta}\right)^2 , \end{aligned} \tag{6.8}$$

and the scalar operators are defined as

$$\begin{aligned} \mathcal{O}_q^{(0)} &= m_q \bar{q} q \,, \\ \mathcal{O}_g^{(0)} &= G^a_{\mu\nu} G^{a,\mu\nu} \,. \end{aligned} \tag{6.9}$$

In this formalism, the matrix element of the spin-independent scattering process between a

DM particle χ and a nucleon N is given by

$$\begin{aligned}\frac{f_N}{m_N} &= \sum_{q=u,d,s,c} f_{Tq} f_q + \frac{3}{4}\left[q(2)+\bar{q}(2)\right]\left(g_q^{(1)}+g_q^{(2)}\right) \\ &\quad -\frac{8\pi}{9\alpha_s} f_{T_G} f_G + \frac{3}{4} G(2)\left(g_G^{(1)}+g_G^{(2)}\right), \end{aligned} \tag{6.10}$$

where f_{Tq}, f_{T_G}, $[q(2)+\bar{q}(2)]$ and $G(2)$ are hadronic matrix elements. The Wilson coefficients of the DM-quark interaction read [55]

$$\begin{aligned} f_q &= \frac{|\tilde{\lambda}_{q3}|^2 m_\chi}{16(m_\phi^2-(m_\chi+m_q)^2)^2}, \\ g_q^{(1)} &= \frac{|\tilde{\lambda}_{q3}|^2 m_\chi}{8(m_\phi^2-(m_\chi+m_q)^2)^2}, \\ g_q^{(2)} &= 0. \end{aligned} \tag{6.11}$$

Note that these coefficients only arise through NLO terms in the expansion of the propagator in the tree-level diagram in Figure 6.1, and thus they are additionally suppressed by a factor of $(m_\phi^2-(m_\chi+m_q)^2)$ when compared to a_u. The Wilson coefficients f_G, $g_G^{(1)}$ and $g_G^{(2)}$ of the gluonic operators $\mathcal{O}_g^{(0)}$ and $\mathcal{O}_{g,\mu\nu}^{(2)}$ can be found in Appendix A.1.

Using the results of [59] we evolve the Wilson coefficients for spin-independent scattering from the new physics scale m_ϕ down to the scattering scale $\mu = 2\,\text{GeV}$. The anomalous dimension and matching matrices can be found in [59]. For the running and decoupling of quark masses and the strong coupling α_s we use the `RunDec` package [60]. The numerical values of the hadronic matrix elements as well as the input quark masses for the RG running can be found in the appendix of [55].

6.2 Direct Detection Constraints

In order to determine the constraints from direct detection experiments on the parameter space of our model, we calculate the spin-dependent as well as the spin-independent scattering cross-sections and compare them to the experimental upper bounds. The strongest constraints on spin-dependent scattering are provided by the PICO-60 experiment [61] and are obtained for WIMP-proton scattering. For spin-independent scattering the world-leading result is provided by the XENON1T [62] experiment.

As the PICO-60 experiment provides limits on spin-dependent WIMP-proton scattering, eq. (6.3) becomes [55, 56]

$$\sigma_{\text{SD}}^p = \frac{3}{16\pi}\frac{m_p^2 m_\chi^2}{(m_p+m_\chi)^2}\left(\Delta u^p a_u\right)^2. \tag{6.12}$$

The spin-independent WIMP-nucleon scattering cross-section is obtained by summing over all nucleons in the nucleus in eq. (6.2) and reads [16, 17]

$$\sigma_{\text{SI}}^N = \frac{4\mu^2}{\pi A^2}|Z f_p + (A-Z) f_n|^2, \tag{6.13}$$

where the reduced mass is defined as $\mu = m_N m_\chi/(m_N+m_\chi)$. Demanding that these cross-

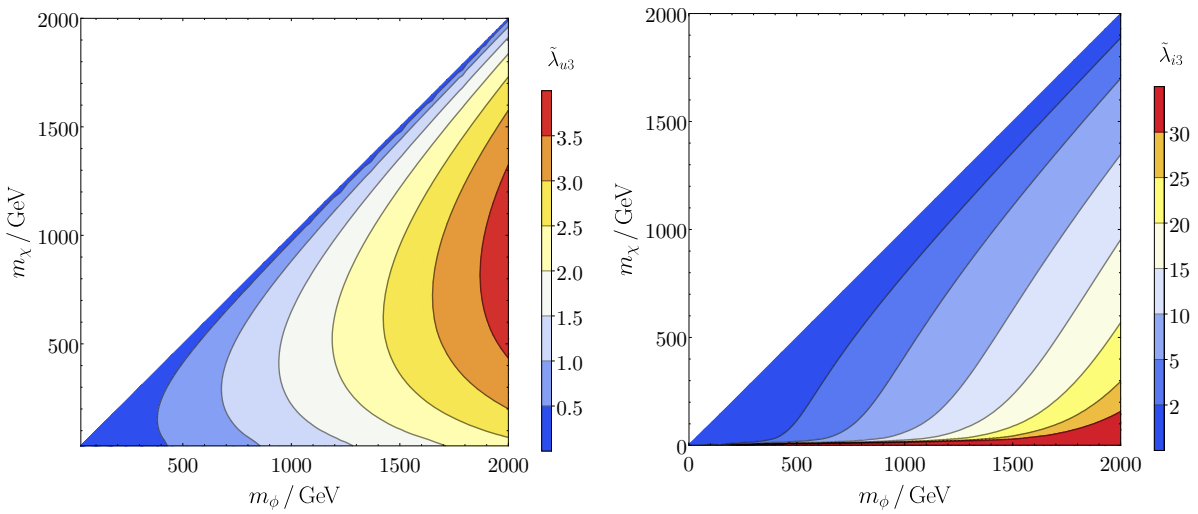

(a) Spin-dependent scattering **(b)** Spin-independent scattering

Figure 6.2: Direct detection limits on $\tilde{\lambda}$ from the PICO-60 and XENON1T experiments. For the latter we have set $\tilde{\lambda}_{u3} = \tilde{\lambda}_{c3} = \tilde{\lambda}_{t3} \equiv \tilde{\lambda}_{i3}$.

sections are below the experimental upper bounds yields limits on the couplings $\tilde{\lambda}_{u3}$, $\tilde{\lambda}_{c3}$ and $\tilde{\lambda}_{t3}$. The results are shown in Figure 6.2.

As we only consider the dominant tree-level contribution to spin-dependent scattering, the PICO-60 constraints solely apply to $\tilde{\lambda}_{u3}$. In Figure 6.2a we see that for large parts of the $m_\phi - m_\chi$ plane the constraints can be completely evaded. For values $m_\phi \gtrsim 1200\,\text{GeV}$ one can always find an m_χ such that the coupling to up-quarks can grow as large as $\tilde{\lambda}_{u3} = 2.0$. As we had restricted the parameters D_i to lie in the range $[0, 2]$ to avoid perturbativity issues, this corresponds to the largest possible value the couplings $\tilde{\lambda}_{i3}$ can take. For even larger values $m_\phi \gtrsim 1500\,\text{GeV}$, the constraints only become relevant in the resonance region $m_\chi \approx m_\phi$ and for small DM masses $m_\chi \lesssim 100\,\text{GeV}$.

In order to analyse the constraints from spin-independent scattering we use the very simple benchmark scenario of a flavour-universal coupling, i.e. we set $\tilde{\lambda}_{u3} = \tilde{\lambda}_{c3} = \tilde{\lambda}_{t3} \equiv \tilde{\lambda}_{i3}$. The results are shown in Figure 6.2b. As can be seen, the constraints are even more lenient in this case. This was to be expected, as the relevant cross-section receives contributions from the dimension-seven and dimension-eight operators given above and is thus highly suppressed by the new physics scale m_ϕ. Only in the resonance region with a mass splitting of at most 10 % between m_ϕ and m_χ the limits become relevant and force the couplings to lie in the range $\tilde{\lambda}_{i3} \leq 2.0$.

We conclude that the direct detection constraints are less stringent than the ones considered in the previous sections and can even be completely evaded over large parts of the parameter space. Due to the Majorana nature of χ they are mostly dominated by spin-dependent scattering.

7 Combined Analysis

In this section we combine our previous results by analysing the validity of our model within the context of all constraints imposed simultaneously. The remaining allowed regions will then yield a global picture of the viable parameter space. We further use this section to analyse the flavour of the DM particle.

7.1 Combined Constraints

The results of the combined application of all constraints are shown in Figure 7.1 and Figure 7.2. Note that the LHC constraints are considered in form of the choices for the masses m_ϕ and m_χ. In both freeze-out scenarios the allowed parameter space is mainly determined by the flavour and relic density constraints. The structure of the coupling matrix λ is also restricted by the choice of the freeze-out scenario, as the hierarchy in λ drives the mass splittings between the dark flavours χ_i.

In Figure 7.1a we show the $|\tilde{\lambda}_{t3}|-|\tilde{\lambda}_{u3}|$ plane for the SFF scenario, i. e. the coupling strengths of the DM particle to the top and up quark. Likewise, Figure 7.1b displays the $|\tilde{\lambda}_{c3}|-|\tilde{\lambda}_{u3}|$ plane. As already discussed in Section 5 the relic abundance constraints reduce the allowed parameter space to the spherical condition

$$\sum_{ij}\sum_{kl}|\tilde{\lambda}_{ki}|^2|\tilde{\lambda}_{lj}|^2 \approx \text{const.}\,, \tag{7.1}$$

for a given pair of m_ϕ and m_χ. In general, this condition restricts the couplings $|\lambda_{ij}|$ to lie on a nine-dimensional sphere. However, in the SFF scenario, the requirement on the DM mass splitting forces the entries in the first two columns of $\tilde{\lambda}$ to be significantly smaller than the

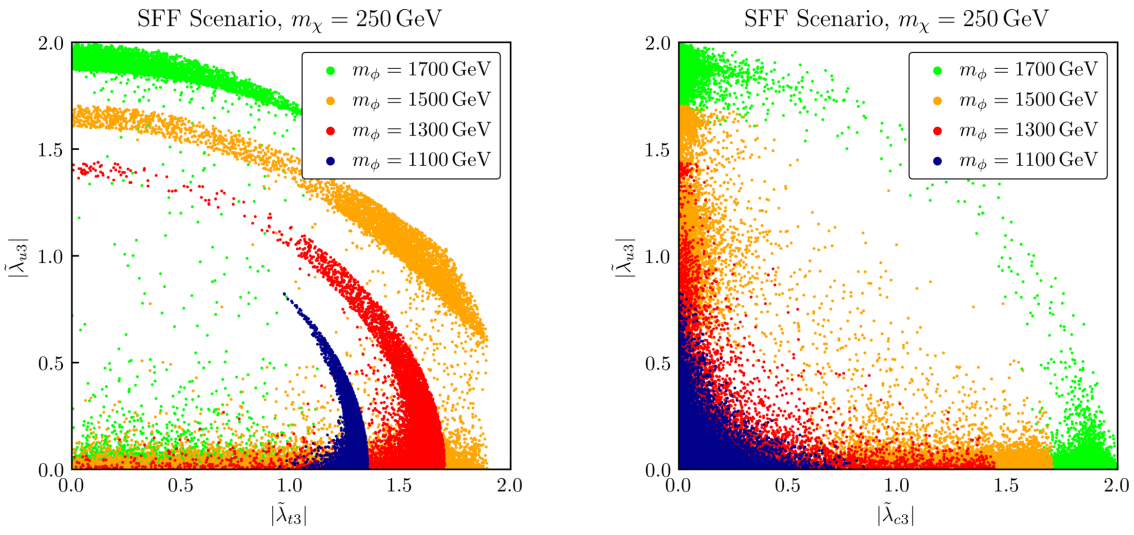

(a) $|\tilde{\lambda}_{t3}|-|\tilde{\lambda}_{u3}|$ plane

(b) $|\tilde{\lambda}_{c3}|-|\tilde{\lambda}_{u3}|$ plane

Figure 7.1: Viable couplings $|\tilde{\lambda}_{i3}|$ for $m_\chi = 250\,\text{GeV}$ and varying m_ϕ within the context of all constraints in the SFF scenario.

entries in the third column. The condition in eq. (7.1) thus reduces to

$$|\tilde{\lambda}_{u3}|^2 + |\tilde{\lambda}_{c3}|^2 + |\tilde{\lambda}_{t3}|^2 \approx \text{const.} \tag{7.2}$$

The $D^0 - \bar{D}^0$ mixing constraints on the other hand, force either $\tilde{\lambda}_{u3}$ or $\tilde{\lambda}_{c3}$ to be small while $\tilde{\lambda}_{t3}$ can be chosen freely. This can be seen in Figure 7.1b, leading to most of the allowed parameter points located close to the axes, with either $|\tilde{\lambda}_{u3}| \simeq 0$ or $|\tilde{\lambda}_{c3}| \simeq 0$. The points with $|\tilde{\lambda}_{u3}| \simeq 0$ are then scattered at the bottom of Figure 7.1a, while the points with $|\tilde{\lambda}_{c3}| \simeq 0$ form the circular bands.

The remaining features in Figure 7.1a can be understood by considering the mass dependence of the DM annihilation cross-section relevant for the thermal freeze-out. As the annihilation cross-section in eq. (5.3) is suppressed by m_ϕ^4, low mediator masses require the DM particle to be top-flavoured in the SFF scenario. This is due to the fact that the phase-space suppression of annihilation channels with top-flavour in the final state is sufficiently large to compensate the cross-section enhancement by the small mediator mass in the denominator. In Figure 7.1a this can be seen explicitly for a mediator mass of $m_\phi = 1100\,\text{GeV}$. For larger m_ϕ the annihilation cross-section becomes sufficiently suppressed such that sizeable contributions to the annihilation channels with up- or charm-flavour in the final state are allowed. At even larger values for m_ϕ top-flavoured DM becomes forbidden, as the above-mentioned phase-space suppression of annihilation into top-quarks in combination with a high m_ϕ-suppression of the annihilation cross section yields a too small relic density. In this case, only up- and charm-flavoured DM is viable.

In Figure 7.2 we show analogous plots for the QDF scenario, with fixed $m_\chi = 250\,\text{GeV}$ and various values of m_ϕ. The emerging patterns are much less clear in this case. The reason is that due to the quasi-degeneracy of the DM flavours, the entries in the three columns of $\tilde{\lambda}$ have to be of similar size. As a result, the plots in Figure 7.2 are two-dimensional projections of the

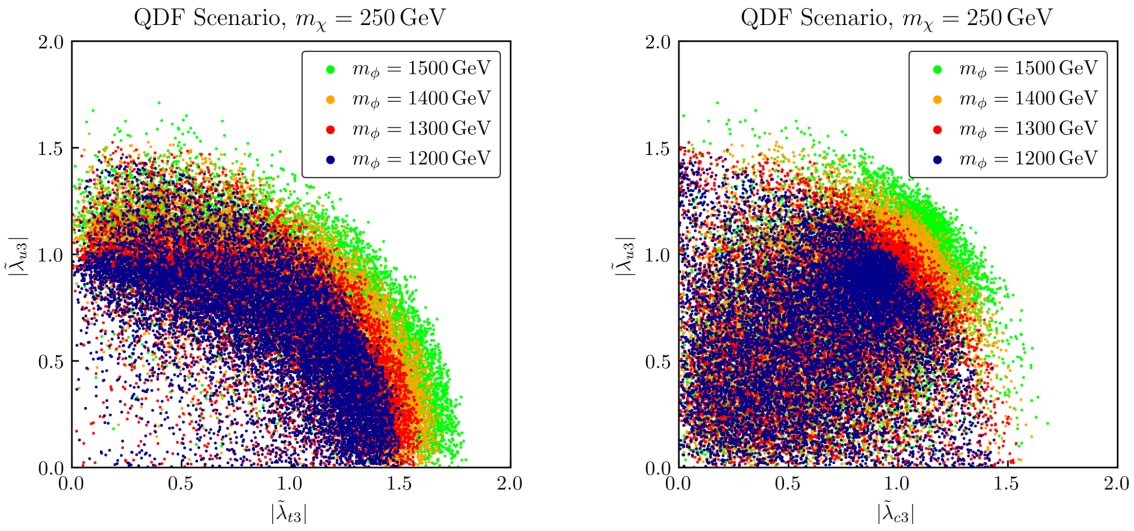

(a) $|\tilde{\lambda}_{t3}| - |\tilde{\lambda}_{u3}|$ plane

(b) $|\tilde{\lambda}_{c3}| - |\tilde{\lambda}_{u3}|$ plane

Figure 7.2: Viable couplings $|\tilde{\lambda}_{i3}|$ within the context of all constraints in the QDF scenario.

nine-dimensional coupling parameter space $|\tilde{\lambda}_{ij}|$. Again we observe the circular bands in the allowed parameter space in Figure 7.2a, stemming from the spherical condition in eq. (7.1). The varying density of parameter points in Figure 7.2a suggests that in the QDF scenario, top-flavoured DM is favoured over up-flavoured DM. The symmetry of Figure 7.2b with respect to interchanging the axes indicates that the constraints do not distinguish between up- and charm-flavour. This was to be expected, as the bounds from direct detection experiments are not relevant for our case of Majorana DM, and the constraints from LHC searches are already accounted for by our choice of mediator and DM masses. Interestingly, the point density in Figure 7.2b is no longer maximal close to the axes, indicating that the $D^0 - \bar{D}^0$ mixing constraints are weaker in the QDF scenario. Indeed, the near degeneracy in the χ_i masses requires a close-to-flavour-universal coupling matrix λ, which in turn suppresses NP contributions to $D^o - \bar{D}^0$ mixing.

7.2 What's your flavour? Tell me, what's your flavour?

The discussion in the previous subsection already contains some aspects related to the flavour of the lightest DM particle χ_3. To be more quantitative, we first define our notion of flavour through the following condition: We call the DM particle χ_3 to be i-flavoured if

$$|\tilde{\lambda}_{i3}| > |\tilde{\lambda}_{j3}|\,, \tag{7.3}$$

with $i \neq j$ and $i, j \in \{u, c, t\}$. In other words, the particle χ_3 has the flavour i if it mainly interacts with the up-type quark of flavour i. With this definition at hand, we now summarise our insights on which DM flavour is favoured by the experimental data.

In order to provide quantitative numerical results for the DM flavour analysis we define

$$n_i = \frac{N_i}{N}\,, \tag{7.4}$$

where N is the total number of allowed parameter points generated in our randomised scan, and N_i the number of allowed points with flavour i for a given constraint. The triple $n_{\text{constr.}} = \{n_u, n_c, n_t\}$ then lists the percentage of viable parameter points with up-, charm- or top-flavoured DM, after imposing that constraint. We stress that our random generation of points prior to the application of the experimental constraints does not favour a specific flavour. The results of this analysis for $m_\phi = 1400\,\text{GeV}$ and several choices for m_χ are shown in Table 7.1. Since in the QDF scenario the dependence on m_χ was found to be much weaker than in the SFF scenario, in the latter case we restrict ourselves to just one value for m_χ.

The constraints on the parameter space from direct detection experiments were found to be marginal in Section 6, and hence it is not surprising that this constraint has no relevant impact on the preferred flavour of DM neither in the SFF nor in the QDF scenario, quantified by n_{direct}. The situation is different for the constraints from $D^0 - \bar{D}^0$ mixing, as the latter amplitude is sensitive to the coupling of the new particles χ_i and ϕ to up and charm quarks. This especially holds true for the SFF scenario, where the mass splitting between the different DM flavours requires the couplings of χ_3 to be dominant, and χ_3 having up- or charm-flavour is thus strongly disfavoured. In the QDF scenario the couplings of the heavier flavours $\chi_{1,2}$ are more relevant so that the tendency towards top-flavoured DM implied by $D^0 - \bar{D}^0$ mixing is weaker in this case. The relic abundance constraints are blind towards the flavour of the DM particle in the QDF scenario, as the initial-state flavours are summed over in eq. (5.3), rendering all nine

Flavour of DM					
scenario	m_χ / GeV	n_{direct} / %	n_{mixing} / %	n_{relic} / %	n_{combined} / %
SFF	200	{33, 33, 34}	{2, 4, 94}	{51, 48, 1}	{29, 71, 0}
	250			{24, 21, 55}	{1, 4, 95}
	300			{27, 24, 49}	{1, 4, 95}
	350			{21, 18, 61}	{1, 2, 97}
QDF	250	{33, 33, 34}	{22, 24, 54}	{33, 33, 34}	{23, 26, 51}

Table 7.1: Numerical results of the flavour analysis for $m_\phi = 1400\,\text{GeV}$. The constraints from direct detection experiments and D mixing do not exhibit a significant dependence on m_χ, so that in the SFF scenario only one numerical result is shown that applies to all four m_χ values.

couplings $|\tilde{\lambda}_{ij}|$ relevant. This sum is omitted in the SFF scenario, since only the lightest flavour is present at freeze-out, so that only the third column of $\tilde{\lambda}$ is constrained. Hence, we encounter strong implications for the flavour of the DM particle, as discussed in detail in the previous subsection. One of them is the aforementioned interplay between the phase-space suppression of annihilation processes into final states with top-flavour and the enhancement by small mediator masses of the annihilation cross-section. Consequently, low mediator masses require the DM particle to be top-flavoured in order to compensate for the enhancement through the phase-space suppression coming from the large top-quark mass. Another important implication is found for small m_χ, where we encounter the opposite behaviour: top-flavour is completely forbidden in this case. This is due to the fact that in the SFF scenario large couplings result in large mass corrections, such that the threshold $m_{\chi_3} < m_t$ is crossed. Then, final states with two top quarks become kinematically forbidden for the annihilation process. Together with the already mentioned phase-space suppression due to the top quark mass, the annihilation cross-section for top-flavoured DM then receives a further suppression by mixing angles and the small couplings to up and charm quarks, yielding a too small relic density. Thus, for such small DM masses up- and charm-flavoured DM is strongly favoured by the cosmological constraints, where up-flavoured DM is slightly more favoured due to the smaller up quark mass and the resulting phase-space enhancement.

Combining the constraints discussed above leads to the distribution of possible DM flavours shown in the last column of Table 7.1. We observe that up- and charm-flavoured DM is largely excluded in the SFF scenario. Only for small DM mass parameters $m_\chi \lesssim 200\,\text{GeV}$ (implying $m_{\chi_3} < m_t$) or large mediator masses $m_\phi \gtrsim 1700\,\text{GeV}$ they become favoured by the relic density constraints for the reasons explained above. For larger DM or smaller mediator masses top-flavoured DM is favoured. While having a much weaker dependence on the mass choice, the QDF scenario shows a similar behaviour. Here, top-flavoured DM again is favoured, however the DM particle can also have up- or charm-flavour.

8 Direct CP Violation in Charm Decays

A central aspect of DMFV models is the structure of the coupling matrix λ and its implications on flavour- and CP-violating observables. While in DMFV models with Dirac DM

flavour-violating interactions were found to be strongly suppressed by the stringent constraints from neutral meson mixing observables [16–19], we have seen in Section 4 that the Majorana nature of DM implies the presence of additional crossed box diagrams that partially cancel the contributions from the standard box diagrams present in both the Dirac and Majorana case. As a consequence, flavour- and CP-violating interactions are less constrained in the Majorana DM model. The conclusion that other new flavour- and CP-violating effects are suppressed therefore no longer holds in the Majorana model.

As the new particles in our model couple to up-type quarks, flavour- and CP-violating D meson decays are expected to receive relevant NP contributions. Of particular interest are the CP asymmetries in $D^0 \to K^+K^-$ and $D^0 \to \pi^+\pi^-$ decays, whose difference ΔA_{CP} was measured by the LHCb collaboration, leading to the discovery of CP violation in charm decays [63]. Notably, the measured value of ΔA_{CP} is significantly larger than its SM expectation. While the latter is plagued by large hadronic uncertainties, this potential discrepancy raises the need for a possible NP explanation. Thus, in this section we discuss if our model is capable of giving rise to a large ΔA_{CP}.

8.1 Theoretical Approach

The LHCb collaboration measured the difference [63]

$$\Delta A_{CP,\,\mathrm{LHCb}}^{\mathrm{dir}} = (-0.157 \pm 0.029)\% \tag{8.1}$$

between the time-integrated direct CP asymmetries in $D^0 \to K^+K^-$ and $D^0 \to \pi^+\pi^-$ decays. The naive SM expectation for this asymmetry can be expressed parametrically as

$$\Delta A_{CP,\,\mathrm{SM}}^{\mathrm{dir}} \sim \mathcal{O}((\alpha_s/\pi)(V_{ub}V_{cb}^*)/(V_{us}V_{cs}^*)) \sim 10^{-4}\,, \tag{8.2}$$

which is an order of magnitude below the experimental value. A more elaborate SM prediction based on QCD light-cone sum rules finds [64]

$$\Delta A_{CP,\,\mathrm{SM}}^{\mathrm{dir}} = (0.02 \pm 0.003)\%\,, \tag{8.3}$$

with a deviation from the data of $4.7\,\sigma$. This discrepancy suggests that the LHCb results might be a hint at NP. Note, however, that the possibility of a significantly larger $\Delta A_{CP,\,\mathrm{SM}}^{\mathrm{dir}}$ has been argued for in the literature [65, 66].

In investigating the possible size of $\Delta A_{CP}^{\mathrm{dir}}$ in our model, we follow the approach in [67] where the naive QCD factorization results for the relevant hadronic matrix elements have been used. For the final state with K^+K^-, for example, it takes the following form

$$\langle K^+K^-|\,(\bar{u}\,\Gamma_1\,s)(\bar{s}\,\Gamma_2\,c)\,|D^0\rangle \approx \langle K^+|\,(\bar{u}\,\Gamma_1\,s)\,|0\rangle\,\langle K^-|\,(\bar{s}\,\Gamma_2\,c)\,|D^0\rangle\ . \tag{8.4}$$

While suffering from large $1/m_c$ corrections, this ansatz enables the calculation of the NP and SM contribution to the CP asymmetry in an effective field theory approach. From [67] we adopt the expression

$$\Delta A_{CP}^{\mathrm{dir}} = A_{K^+K^-}^{d} - A_{\pi^+\pi^-}^{d}\,, \tag{8.5}$$

where the direct CP asymmetry for the final state f is given by

$$A_f^d = 2\,r_f \sin\delta_f \sin\phi_f\,, \tag{8.6}$$

under the assumption that r_f is small. Here, δ_f and ϕ_f are the differences of strong and weak phases, respectively, of the two interfering decay amplitudes, and r_f is their relative magnitude. The general expression of r_f and ϕ_f as an expansion of Wilson coefficients for the relevant set of $\Delta F = 1$ operators reads [67]

$$r_f e^{i\phi_f} \simeq \left(C_1^{(1)p} + \frac{C_2^{(1)p}}{N_c}\right)^{-1} \left(\frac{(C_2^{(1)p})_{\rm NP}}{N_c} + C_4^{(1)} + \frac{C_3^{(1)}}{N_c} - \frac{C_{10}^{(1)}}{2} - \frac{C_9^{(1)}}{2N_c} - \frac{3\alpha_s}{4\pi}\frac{N_c^2-1}{N_c^2} C_{8g}^{(1)} + \chi_f \left(C_6^{(1)} + \frac{C_5^{(1)}}{N_c} - \frac{C_8^{(1)}}{2} - \frac{C_7^{(1)}}{2N_c} - \frac{\alpha_s}{4\pi}\frac{N_c^2-1}{N_c^2} C_{8g}^{(1)}\right) + (C_i^{(1)} \leftrightarrow \tilde{C}_i^{(1)})\right), \tag{8.7}$$

where $N_c = 3$ is the number of colours and γ_f are the chirality factors of the final states f, which are approximately

$$\gamma_K \simeq \frac{2m_K^2}{m_c m_s}, \qquad \gamma_\pi \simeq \frac{2m_\pi^2}{m_c(m_d + m_u)}. \tag{8.8}$$

Note that we have dropped the Wilson coefficients of scalar operators in eq. (8.7), as they are absent in our model and their RG running is decoupled from the $\Delta F = 1$ operators included above. A complete list of the operators contributing to the CP asymmetry can be found in [67].

In our model, the only NP contribution to $\Delta A_{CP}^{\rm dir}$ arises through gluon penguins as shown in Figure 8.1. We determine the following relevant NP contributions

$$\begin{aligned}
\tilde{C}_6^{(1)} &= \frac{\alpha_s}{4\pi} \sum_i \tilde{\lambda}_{ui} \tilde{\lambda}_{ci}^* \frac{1}{8m_\phi^2} u(x), \\
\tilde{C}_3^{(1)} &= \tilde{C}_5^{(1)} = -\frac{1}{N_c} \tilde{C}_4^{(1)} = -\frac{1}{N_c} \tilde{C}_6^{(1)}, \\
\tilde{C}_{8g}^{(1)} &= \sum_i \tilde{\lambda}_{ui} \tilde{\lambda}_{ci}^* \frac{1}{4m_\phi^2} v(x),
\end{aligned} \tag{8.9}$$

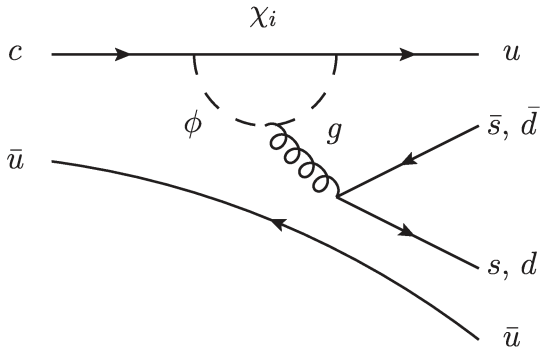

Figure 8.1: Penguin diagram contributing to $D^0 \to K^+K^-$ and $D^0 \to \pi^+\pi^-$.

with the loop functions

$$u(x) = -\frac{2-7x+11x^2}{36(1-x)^3} - \frac{x^3}{6(1-x)^4}\log(x)\,,$$
$$v(x) = \frac{1-5x-2x^2}{24(1-x)^3} - \frac{x^2}{4(1-x)^4}\log(x)\,, \tag{8.10}$$

and $x = m_\chi^2/m_\phi^2$ [67]. The Wilson coefficient $C_1^{(1)p}$ is generated at the electroweak scale, where the W boson is integrated out, and reads

$$C_1^{(1)p} = \lambda_p \frac{G_F}{\sqrt{2}}\,, \tag{8.11}$$

with $\lambda_p = V_{cp}V_{up}^*$ and $p = s$ for $f = K$ or $p = d$ for $f = \pi$, respectively. Following [67–69] we assume $\mathcal{O}(1)$ strong phase differences.

For the numerical analysis we use leading-order renormalization group running to evolve the Wilson coefficients from the NP scale down to the meson scale $\mu \approx m_D$. The anomalous dimensions are adopted from [67], and for the running of the quark masses and the strong coupling α_s we again use the `RunDec` package [60]. The values for the CKM elements are obtained from the UTfit website [70]. Due to the large uncertainties stemming from the naive factorization approach we follow [67–69] and allow for an enhancement factor of two for the ratio r_f.

8.2 Results

In order to estimate the size of the CP asymmetry $\Delta A_{CP}^{\text{dir}}$ generated in our model, we use parameter points that fulfil the constraints discussed in the previous sections at the 2σ level. We then determine the range of possible $\Delta A_{CP}^{\text{dir}}$ values spanned by these points, both assuming no enhancement relative to the naive factorization result, and allowing for a factor of two enhancement.

The results for the two freeze-out scenarios are gathered in Figure 8.2. In the QDF scenario in Figure 8.2a the $1/m_\phi^2$ suppression of the Wilson coefficients listed in eq. (8.9) determines the mediator mass dependence of the CP asymmetry $\Delta A_{CP}^{\text{dir}}$. In the QCD factorization limit, values for $\Delta A_{CP}^{\text{dir}} \simeq -0.1\%$ can be reached for low mediator masses $m_\phi = 1\,\text{TeV}$, bringing the CP asymmetry in agreement with the 2σ experimental region. Allowing for a factor of two enhancement of r_f, the experimental 2σ region can be reached for mediator masses $m_\phi \lesssim 1600\,\text{GeV}$ As the allowed region grows with decreasing mediator masses m_ϕ, it crosses the 1σ band for $m_\phi \lesssim 1400\,\text{GeV}$. For smaller masses $m_\phi \lesssim 1200\,\text{GeV}$, even the central value of the LHCb measurement can be reached. We conclude that the QDF scenario is capable of explaining the large value of $\Delta A_{CP}^{\text{dir}}$ measured by the LHCb collaboration.

In Figure 8.2b we show the results for the SFF scenario. In contrast to the QDF scenario, here $\Delta A_{CP}^{\text{dir}}$ increases for an increasing mediator mass m_ϕ up to a value of $m_\phi \simeq 1600\,\text{GeV}$ and then starts to decrease. This quite counter-intuitive result can be understood well with our results from Section 7 and Figure 7.1a in particular. We had seen there that for a growing mediator mass the DM particle is more likely up- or charm-flavoured, i.e. increasing mediator masses lead to increasing values of at least one of the relevant couplings $|\tilde{\lambda}_{u3}|$ and $|\tilde{\lambda}_{c3}|$. Hence, $\Delta A_{CP}^{\text{dir}}$ also grows with an increasing value for m_ϕ in the SFF scenario. As we had limited the

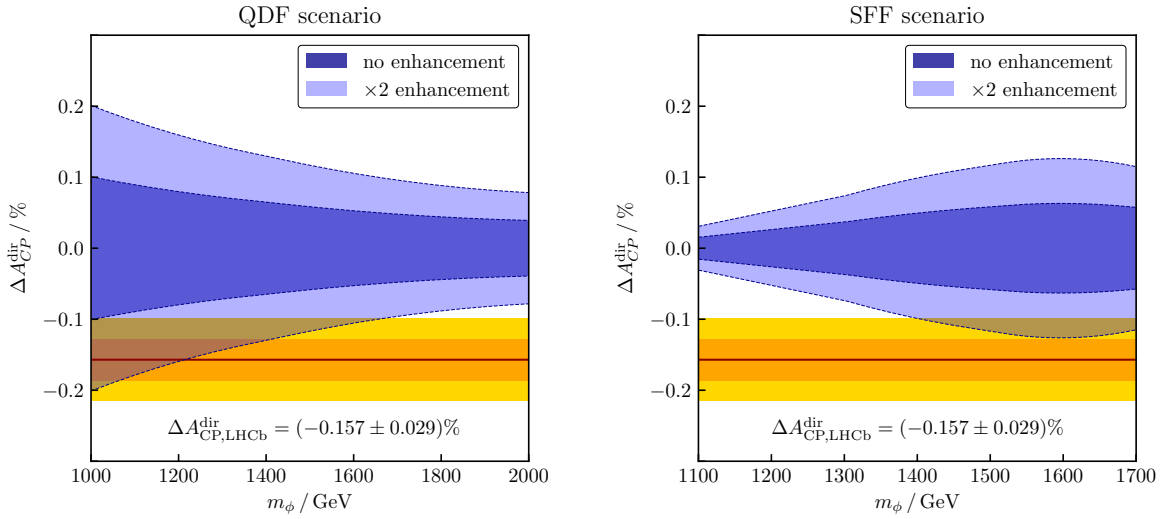

(a) QDF scenario, $m_\chi = 350\,\text{GeV}$ **(b)** SFF scenario, $m_\chi = 250\,\text{GeV}$

Figure 8.2: $\Delta A_{CP}^{\rm dir}$ in dependence of m_ϕ in the two freeze-out scenarios. The blue contours correspond to the ranges covered by our model, as discussed in the text. The red, orange and yellow bands display the LHCb measurement with its 1σ and 2σ uncertainty bands.

maximum value of the couplings $|\tilde{\lambda}_{i3}|$, $\Delta A_{CP}^{\rm dir}$ encounters a suppression for even larger mediator masses $m_\phi \gtrsim 1600\,\text{GeV}$. In the SFF scenario the maximal values of $\Delta A_{CP}^{\rm dir}$ are smaller than in the QDF scenario. Still, when allowing for a factor of two enhancement the allowed region crosses the 2σ band for masses $m_\phi \gtrsim 1400\,\text{GeV}$ and touches the 1σ band at $m_\phi \simeq 1600\,\text{GeV}$. In the strict QCD factorization limit without enhancement factor, the SFF scenario is not able to resolve the discrepancy in $\Delta A_{CP}^{\rm dir}$.

9 Summary and Outlook

In this paper we studied a simplified model of flavoured DM within the DMFV framework [16] in which the DM relic is formed by the lightest flavour of a Majorana fermion flavour triplet χ coupling to SM up-type quarks u_R via a coloured scalar mediator ϕ. The 3×3 coupling matrix λ mediating this interaction constitutes the only new source of flavour and CP violation beyond the SM Yukawa couplings in the DMFV framework. In contrast to the case of Dirac DMFV models investigated in [16–20], in the Majorana scenario the underlying flavour symmetry in the dark sector is $O(3)_\chi$. As a consequence, the coupling matrix λ contains more physical parameters.

In order to constrain the structure of λ and determine the viable parameter space of the model, we investigated the constraints from LHC searches for new particles, $D^0 - \bar{D}^0$ mixing observables, cosmological constraints on the DM relic density, and limits from DM direct detection experiments. Our main findings can be summarised as follows:

- The strongest limits from LHC searches on the model are obtained from searches for

SUSY squarks, giving rise to the final states tops + $\not{E}_T$ and $jj + \not{E}_T$. Recasting the limits obtained by CMS, using 136 fb^{-1} of run-2 data, we determined the bounds on the masses m_χ and m_ϕ, depending on the new coupling parameters. We found that the LHC phenomenology is strongly affected by the Majorana nature of χ, as an additional same-sign $\phi\phi$ production channel arises in this case. The existing experimental cross-section limits can be fulfilled by choosing $0 \leq D_3 \leq 1.5$ and $0 \leq D_1, D_2 \leq 0.5$ for mediator masses $m_\phi \gtrsim 1\,\text{TeV}$. While this choice makes a case for top-flavoured DM, it is also possible to fulfil the LHC constraints with larger D_1 and D_2 but small m_χ due to the suppression of the same-sign contributions.

- The Majorana nature of χ, inducing same-sign $\phi\phi$ pair production, gives rise to the new final-state signature of two positively charged top quarks in association with missing transverse energy, $tt+\not{E}_T$. In 14 TeV pp collisions, we predicted production cross-sections of this final state in the multi-fb regime, making it a promising smoking-gun signature for future LHC runs.

- The measurements of $D^0 - \bar{D}^0$ mixing observables require the combination of the NP couplings to up and charm quarks to be small. Choosing $0 \leq D_1, D_2 \leq 0.5$ fulfils the constraints while allowing for large mixing angles θ_{ij} and a freely chosen coupling D_3. Relative to the case of Dirac DM, the Majorana nature of χ generates an additional mixing diagram with crossed fermion lines. The latter interferes destructively with the contribution from standard box diagrams, leading to relaxed constraints on the flavour-violating couplings relative to the Dirac model.

- The thermal freeze-out of DM depends on the mass hierarchy among the dark flavours χ. Following the studies of flavoured Dirac DM, we investigated two limiting cases: the QDF scenario in which the dark flavours are quasi-degenerate and therefore all three states are present at freeze-out, and the SFF scenario in which the heavier flavours are split significantly from the lightest and thus only the latter contributes to the effective annihilation cross-section. The relic abundance constraints impose a spherical condition on the elements of the matrix λ. As we restricted the couplings D_i to lie within the range $[0, 2]$, this poses a lower bound on the DM mass m_χ. In the SFF scenario we encountered a strong m_χ dependence, with an additional upper bound on the DM mass m_χ.

- The constraints from DM direct detection experiments are significantly weaker for Majorana DM than for the Dirac case, as the dominant spin-independent contributions to the DM-nucleus scattering cross-section are absent. Consequently, the constraints on the parameter space are rather mild and mainly dominated by contributions from spin-dependent scattering.

In our subsequent combined analysis we investigated the interplay of these constraints in limiting the viable parameter space for the coupling matrix λ. In both freeze-out scenarios the interplay between the relic density and $D^0 - \bar{D}^0$ mixing constraints mainly determines the allowed regions of parameter space. In the QDF scenario the former constraint reduces to a spherical condition om the coupling parameters, without a qualitative dependence on the choice of the masses. The SFF condition on the other hand only allows for sharp bands in each plane $|\tilde{\lambda}_{i3}| - |\tilde{\lambda}_{j3}|$, as the couplings of the third DM generation χ_3 are dominant in this scenario. We further identified a strong dependence on the DM mass m_χ implied by the relic abundance constraint.

We then determined the flavour of the lightest DM field χ_3, i. e. the quark to which it couples mostly. In the SFF scenario up and charm flavour are unlikely for $m_\chi \gtrsim 250\,\text{GeV}$, and χ_3 carries top flavour in most of the allowed parameter space. Contrary, for smaller DM masses only up or charm flavour is allowed, since in that case DM annihilation into final states with two top quarks is kinematically forbidden. While the QDF scenario favours top-flavoured DM, a significant part of the allowed parameter space still corresponds to up and charm flavour.

In the last part of this paper we investigated the possible amount of CP violation in charm decays induced in our model. The CP asymmetry $\Delta A_{CP}^{\text{dir}}$ in $D^0 \to K^+K^-$ and $D^0 \to \pi^+\pi^-$ decays has been measured by the LHCb collaboration with a surprisingly large value, making a NP contribution plausible. Both the QDF and SFF scenarios are capable of significantly enhancing $\Delta A_{CP}^{\text{dir}}$ w. r. t. its naive SM expectation. While in the SFF scenario a modest deviation from the naive QCD factorization limit is also required to bring our model in agreement with the data, in the QDF scenario values for $\Delta A_{CP}^{\text{dir}}$ as large as 10^{-3} can be reached even in the strict QCD factorization limit.

In conclusion, the DMFV framework provides an elegant connection of the DM problem to one of the least understood aspects of the SM: flavour. Introducing the DM flavour triplet as Majorana fermions, instead of Dirac fermions as done in the previous literature, turns out to have several phenomenological advantages. On the one hand, the stringent constraints from $D^0 - \bar{D}^0$ mixing and DM direct detection experiments can be softened considerably, opening up additional viable parameter space. On the other hand, the Majorana nature of DM leads to the prediction of the rather striking signature of a pair of same-sign top quarks in association with missing transverse energy at the LHC. It can also provide a NP origin for large values of the CP asymmetry $\Delta A_{CP}^{\text{dir}}$ in charm decays, without the need for large hadronic enhancement effects. Upcoming experimental measurements will hence be able to shed light on the nature of DM and its flavour.

Acknowledgements We thank Jan Heisig, Simon Kast, Michael Krämer, Kirtimaan Mohan, Margarete Mühlleitner, and Mustafa Tabet for useful discussions. This work is supported by the Deutsche Forschungsgemeinschaft (DFG, German Research Foundation) under grant 396021762 – TRR 257. H.A. acknowledges the scholarship and support he receives from the Avicenna-Studienwerk e.V., and the support of the doctoral school "Karlsruhe School of Elementary and Astroparticle Physics: Science and Technology (KSETA)".

A Direct Detection

A.1 Gluonic Wilson Coefficients

The Wilson coefficents f_G, $g_G^{(1)}$ and $g_G^{(2)}$ from eq. (6.10) read [55]

$$
\begin{aligned}
f_G = \sum_{i=u,c,t} \alpha_s |\tilde{\lambda}_{i3}|^2 m_{\chi_3} \Big[& -12 m_i^2 m_\phi^4 m_{\chi_3}^2 (m_i^2 - m_\phi^2 + m_{\chi_3}^2) \Lambda_i(m_{\chi_3}^2; m_i, m_\phi) \\
& - (m_i - m_\phi - m_{\chi_3})(m_i + m_\phi - m_{\chi_3})(m_i - m_\phi + m_{\chi_3}) \\
& \times (m_i + m_\phi + m_{\chi_3}) \{ m_i^6 - 3 m_i^4 (2 m_\phi^2 + m_{\chi_3}^2) \\
& + m_i^2 (3 m_\phi^4 + 2 m_\phi^2 m_{\chi_3}^2 + 3 m_{\chi_3}^4) + (m_\phi^2 - m_{\chi_3}^2)^2 (2 m_\phi^2 - m_{\chi_3}^2) \} \Big] \\
& \times \frac{(m_i - m_\phi + m_{\chi_3})^{-3} (m_i + m_\phi + m_{\chi_3})^{-3}}{192 \pi m_\phi^2 (m_i - m_\phi - m_{\chi_3})^3 (m_i + m_\phi - m_{\chi_3})^3} \,,
\end{aligned}
\tag{A.1}
$$

$$
\begin{aligned}
\frac{g_G^{(2)}}{m_{\chi_3}^2} = \sum_{i=u,c,t} \alpha_s |\tilde{\lambda}_{i3}|^2 \Big[& 2 m_{\chi_3}^2 \{ 10 m_{\chi_3}^4 (m_i^6 - m_\phi^6) + m_{\chi_3}^8 (m_i^2 - 5 m_\phi^2) - 5 m_{\chi_3}^2 (m_i^2 - m_\phi^2)^3 \\
& \times (m_i^2 + m_\phi^2) + (m_i^2 - m_\phi^2)^5 + 2 m_{\chi_3}^6 (-4 m_i^4 + 2 m_i^2 m_\phi^2 + 5 m_\phi^4) + m_{\chi_3}^{10} \} \\
& \times \Lambda_i(m_{\chi_3}^2; m_i, m_\phi) - (m_i - m_\phi - m_{\chi_3})(m_i + m_\phi - m_{\chi_3})(m_i - m_\phi + m_{\chi_3}) \\
& \times (m_i + m_\phi + m_{\chi_3}) \Big\{ 7 m_{\chi_3}^4 (m_i^4 - m_\phi^4) - 2 m_{\chi_3}^6 (m_i^2 - 4 m_\phi^2) - 2 m_{\chi_3}^2 (m_i^2 - m_\phi^2)^3 \\
& + 2 (m_i^4 - 2 m_i^2 (m_\phi^2 + m_{\chi_3}^2) + (m_\phi^2 - m_{\chi_3}^2)^2)^2 \log(\frac{m}{m_\phi}) - 3 m_{\chi_3}^8 \Big\} \Big] \\
& \times \frac{(m_i - m_\phi + m_{\chi_3})^{-3} (m_i + m_\phi + m_{\chi_3})^{-3}}{48 \pi m_{\chi_3}^5 (m_i - m_\phi - m_{\chi_3})^3 (m_i + m_\phi - m_{\chi_3})^3} \,,
\end{aligned}
\tag{A.2}
$$

$$
\begin{aligned}
\frac{g_G^{(1)}}{m_{\chi_3}} = \sum_{i=u,c,t} \alpha_s |\tilde{\lambda}_{i3}|^2 \Big[& 2 m_{\chi_3}^2 (3 m_{\chi_3}^2 (m_\phi^4 - m_i^4) + m_{\chi_3}^4 (5 m_i^2 + m_\phi^2) + (m_i^2 - m_\phi^2)^3 - 3 m_{\chi_3}^6) \\
& \times \Lambda_i(m_{\chi_3}^2; m_i, m_\phi) + 2 (m_i + m_\phi - m_{\chi_3})(m_i - m_\phi + m_{\chi_3})(m_i + m_\phi + m_{\chi_3}) \\
& \Big\{ m_{\chi_3}^2 (m_i - m_\phi - m_{\chi_3})(m_i^2 - m_\phi^2 - 3 m_{\chi_3}^2) - (m_i + m_\phi - m_{\chi_3})(m_i - m_\phi + m_{\chi_3}) \\
& \times (-m_i + m_\phi + m_{\chi_3})^2 (m_i + m_\phi + m_{\chi_3}) \log(\frac{m_i}{m_\phi}) \Big\} \Big] \\
& \times \frac{(-m_i + m_\phi + m_{\chi_3})^{-2} (m_i + m_\phi + m_{\chi_3})^{-2}}{192 \pi m_{\chi_3}^4 (m_i + m_\phi - m_{\chi_3})^2 (m_i - m_\phi + m_{\chi_3})^2} \,,
\end{aligned}
\tag{A.3}
$$

with

$$\Lambda_i(m_{\chi_3}^2; m_i, m_\phi) = \frac{\lambda_i}{m_{\chi_3}^2} \log\left(\frac{m_i^2 + \lambda_i + m_\phi^2 - m_{\chi_3}^2}{2 m_i m_\phi}\right)$$
$$\lambda_i = \sqrt{m_i^4 - 2m_i^2 m_\phi^2 - 2m_i^2 m_{\chi_3}^2 + m_\phi^4 - 2m_\phi^2 m_{\chi_3}^2 + m_{\chi_3}^4}\,. \tag{A.4}$$

References

[1] G. Arcadi, M. Dutra, P. Ghosh, M. Lindner, Y. Mambrini, M. Pierre et al., *The waning of the WIMP? A review of models, searches, and constraints*, *Eur. Phys. J. C* **78** (2018) 203 [1703.07364].

[2] J. Kile and A. Soni, *Flavored Dark Matter in Direct Detection Experiments and at LHC*, *Phys. Rev. D* **84** (2011) 035016 [1104.5239].

[3] J. F. Kamenik and J. Zupan, *Discovering Dark Matter Through Flavor Violation at the LHC*, *Phys. Rev. D* **84** (2011) 111502 [1107.0623].

[4] B. Batell, J. Pradler and M. Spannowsky, *Dark Matter from Minimal Flavor Violation*, *JHEP* **08** (2011) 038 [1105.1781].

[5] P. Agrawal, S. Blanchet, Z. Chacko and C. Kilic, *Flavored Dark Matter, and Its Implications for Direct Detection and Colliders*, *Phys. Rev. D* **86** (2012) 055002 [1109.3516].

[6] B. Batell, T. Lin and L.-T. Wang, *Flavored Dark Matter and R-Parity Violation*, *JHEP* **01** (2014) 075 [1309.4462].

[7] J. Kile, *Flavored Dark Matter: A Review*, *Mod. Phys. Lett. A* **28** (2013) 1330031 [1308.0584].

[8] L. Lopez-Honorez and L. Merlo, *Dark matter within the minimal flavour violation ansatz*, *Phys. Lett. B* **722** (2013) 135 [1303.1087].

[9] A. Kumar and S. Tulin, *Top-flavored dark matter and the forward-backward asymmetry*, *Phys. Rev. D* **87** (2013) 095006 [1303.0332].

[10] Y. Zhang, *Top Quark Mediated Dark Matter*, *Phys. Lett. B* **720** (2013) 137 [1212.2730].

[11] A. J. Buras, P. Gambino, M. Gorbahn, S. Jager and L. Silvestrini, *Universal unitarity triangle and physics beyond the standard model*, *Phys. Lett. B* **500** (2001) 161 [hep-ph/0007085].

[12] G. D'Ambrosio, G. F. Giudice, G. Isidori and A. Strumia, *Minimal flavor violation: An Effective field theory approach*, *Nucl. Phys. B* **645** (2002) 155 [hep-ph/0207036].

[13] A. J. Buras, *Minimal flavor violation*, *Acta Phys. Polon. B* **34** (2003) 5615 [hep-ph/0310208].

[14] R. S. Chivukula and H. Georgi, *Composite Technicolor Standard Model*, *Phys. Lett. B* **188** (1987) 99.

[15] L. J. Hall and L. Randall, *Weak scale effective supersymmetry*, *Phys. Rev. Lett.* **65** (1990) 2939.

[16] P. Agrawal, M. Blanke and K. Gemmler, *Flavored dark matter beyond Minimal Flavor Violation*, *JHEP* **10** (2014) 072 [1405.6709].

[17] M. Blanke and S. Kast, *Top-Flavoured Dark Matter in Dark Minimal Flavour Violation*, *JHEP* **05** (2017) 162 [1702.08457].

[18] T. Jubb, M. Kirk and A. Lenz, *Charming Dark Matter*, *JHEP* **12** (2017) 010 [1709.01930].

[19] M. Blanke, S. Das and S. Kast, *Flavoured Dark Matter Moving Left*, *JHEP* **02** (2018) 105 [1711.10493].

[20] M.-C. Chen, J. Huang and V. Takhistov, *Beyond Minimal Lepton Flavored Dark Matter*, *JHEP* **02** (2016) 060 [1510.04694].

[21] M. Blanke, G. F. Giudice, P. Paradisi, G. Perez and J. Zupan, *Flavoured Naturalness*, *JHEP* **06** (2013) 022 [1302.7232].

[22] A. Chakraborty, M. Endo, B. Fuks, B. Herrmann, M. M. Nojiri, P. Pani et al., *Flavour-violating decays of mixed top-charm squarks at the LHC*, *Eur. Phys. J. C* **78** (2018) 844 [1808.07488].

[23] M. Blanke, P. Pani, G. Polesello and G. Rovelli, *Single-top final states as a probe of top-flavoured dark matter models at the LHC*, *JHEP* **01** (2021) 194 [2010.10530].

[24] H. Führ and Z. Rzeszotnik, *A note on factoring unitary matrices*, *Linear Algebra and its Applications* **547** (2018) 32.

[25] M. Blanke, A. J. Buras, A. Poschenrieder, S. Recksiegel, C. Tarantino, S. Uhlig et al., *Another look at the flavour structure of the littlest Higgs model with T-parity*, *Phys. Lett. B* **646** (2007) 253 [hep-ph/0609284].

[26] L. Autonne and L. C. Autonne, *Sur les matrices hypohermitiennes et sur les matrices unitaires*. A. Rey, 1915.

[27] T. Takagi, *On an algebraic problem reluted to an analytic theorem of carathéodory and fejér and on an allied theorem of landau*, *Japanese journal of mathematics: transactions and abstracts* **1** (1924) 83.

[28] M. Papucci, A. Vichi and K. M. Zurek, *Monojet versus the rest of the world I: t-channel models*, *JHEP* **11** (2014) 024 [1402.2285].

[29] A. D. Martin, W. J. Stirling, R. S. Thorne and G. Watt, *Parton distributions for the LHC*, *Eur. Phys. J. C* **63** (2009) 189 [0901.0002].

[30] T. Hurth and W. Porod, *Flavour violating squark and gluino decays*, *JHEP* **08** (2009) 087 [0904.4574].

[31] P. Agrawal and C. Frugiuele, *Mixing stops at the LHC*, *JHEP* **01** (2014) 115 [1304.3068].

[32] M. Arana-Catania, S. Heinemeyer and M. J. Herrero, *Updated Constraints on General Squark Flavor Mixing*, *Phys. Rev. D* **90** (2014) 075003 [1405.6960].

[33] M. Backović, A. Mariotti and M. Spannowsky, *Signs of Tops from Highly Mixed Stops*, *JHEP* **06** (2015) 122 [1504.00927].

[34] M. Blanke, B. Fuks, I. Galon and G. Perez, *Gluino Meets Flavored Naturalness*, *JHEP* **04** (2016) 044 [1512.03813].

[35] CMS collaboration, *Search for supersymmetry in proton-proton collisions at 13 TeV in final states with jets and missing transverse momentum*, *JHEP* **10** (2019) 244 [1908.04722].

[36] J. Alwall, R. Frederix, S. Frixione, V. Hirschi, F. Maltoni, O. Mattelaer et al., *The automated computation of tree-level and next-to-leading order differential cross sections, and their matching to parton shower simulations*, *JHEP* **07** (2014) 079 [1405.0301].

[37] A. Alloul, N. D. Christensen, C. Degrande, C. Duhr and B. Fuks, *FeynRules 2.0 - A complete toolbox for tree-level phenomenology*, *Comput. Phys. Commun.* **185** (2014) 2250 [1310.1921].

[38] CMS collaboration, *Search for physics beyond the standard model in events with jets and two same-sign or at least three charged leptons in proton-proton collisions at* $\sqrt{s} = 13$ *TeV*, *Eur. Phys. J. C* **80** (2020) 752 [2001.10086].

[39] G. Buchalla, A. J. Buras and M. E. Lautenbacher, *Weak decays beyond leading logarithms*, *Rev. Mod. Phys.* **68** (1996) 1125 [hep-ph/9512380].

[40] A. J. Buras, *Weak Hamiltonian, CP violation and rare decays*, hep-ph/9806471.

[41] A. Crivellin and M. Davidkov, *Do squarks have to be degenerate? Constraining the mass splitting with Kaon and D mixing*, *Phys. Rev. D* **81** (2010) 095004 [1002.2653].

[42] Flavour Lattice Averaging Group collaboration, *FLAG Review 2019: Flavour Lattice Averaging Group (FLAG)*, *Eur. Phys. J. C* **80** (2020) 113 [1902.08191].

[43] N. Carrasco et al., $D^0 - \bar{D}^0$ *mixing in the standard model and beyond from* $N_f = 2$ *twisted mass QCD*, *Phys. Rev. D* **90** (2014) 014502 [1403.7302].

[44] A. J. Buras, S. Jager and J. Urban, *Master formulae for Delta F=2 NLO QCD factors in the standard model and beyond*, *Nucl. Phys. B* **605** (2001) 600 [hep-ph/0102316].

[45] Particle Data Group collaboration, *Review of Particle Physics*, *PTEP* **2020** (2020) 083C01.

[46] HFLAV collaboration, *Averages of b-hadron, c-hadron, and* τ*-lepton properties as of 2018*, 1909.12524.

[47] A. A. Petrov, *Long-distance effects in charm mixing*, in *6th International Workshop on Charm Physics*, 12, 2013, 1312.5304.

[48] Planck collaboration, *Planck 2018 results. VI. Cosmological parameters*, *Astron. Astrophys.* **641** (2020) A6 [1807.06209].

[49] G. Steigman, B. Dasgupta and J. F. Beacom, *Precise Relic WIMP Abundance and its Impact on Searches for Dark Matter Annihilation*, *Phys. Rev. D* **86** (2012) 023506 [1204.3622].

[50] J. D. Wells, *Annihilation cross-sections for relic densities in the low velocity limit*, hep-ph/9404219.

[51] K. Griest and D. Seckel, *Three exceptions in the calculation of relic abundances*, *Phys. Rev. D* **43** (1991) 3191.

[52] G. Servant and T. M. P. Tait, *Is the lightest Kaluza-Klein particle a viable dark matter candidate?*, *Nucl. Phys. B* **650** (2003) 391 [hep-ph/0206071].

[53] P. Agrawal, Z. Chacko, C. Kilic and R. K. Mishra, *A Classification of Dark Matter Candidates with Primarily Spin-Dependent Interactions with Matter*, 1003.1912.

[54] M. Garny, A. Ibarra and S. Vogl, *Signatures of Majorana dark matter with t-channel mediators*, *Int. J. Mod. Phys. D* **24** (2015) 1530019 [1503.01500].

[55] K. A. Mohan, D. Sengupta, T. M. P. Tait, B. Yan and C. P. Yuan, *Direct detection and LHC constraints on a t-channel simplified model of Majorana dark matter at one loop*, *JHEP* **05** (2019) 115 [1903.05650].

[56] M. Freytsis and Z. Ligeti, *On dark matter models with uniquely spin-dependent detection possibilities*, *Phys. Rev. D* **83** (2011) 115009 [1012.5317].

[57] J. Hisano, K. Ishiwata and N. Nagata, *Gluon contribution to the dark matter direct detection*, *Phys. Rev. D* **82** (2010) 115007 [1007.2601].

[58] R. J. Hill and M. P. Solon, *Standard Model anatomy of WIMP dark matter direct detection I: weak-scale matching*, *Phys. Rev. D* **91** (2015) 043504 [1401.3339].

[59] R. J. Hill and M. P. Solon, *Standard Model anatomy of WIMP dark matter direct detection II: QCD analysis and hadronic matrix elements*, *Phys. Rev. D* **91** (2015) 043505 [1409.8290].

[60] K. G. Chetyrkin, J. H. Kuhn and M. Steinhauser, *RunDec: A Mathematica package for running and decoupling of the strong coupling and quark masses*, *Comput. Phys. Commun.* **133** (2000) 43 [hep-ph/0004189].

[61] PICO collaboration, *PICO-60 Results and PICO-40L Status*, *J. Phys. Conf. Ser.* **1468** (2020) 012043.

[62] XENON collaboration, *XENON1T results from 1 tonne×year WIMP search*, *PoS* **NOW2018** (2018) 094.

[63] LHCb collaboration, *Observation of CP Violation in Charm Decays*, *Phys. Rev. Lett.* **122** (2019) 211803 [1903.08726].

[64] A. Khodjamirian and A. A. Petrov, *Direct CP asymmetry in $D \to \pi^-\pi^+$ and $D \to K^-K^+$ in QCD-based approach*, *Phys. Lett. B* **774** (2017) 235 [1706.07780].

[65] J. Brod, A. L. Kagan and J. Zupan, *Size of direct CP violation in singly Cabibbo-suppressed D decays*, *Phys. Rev. D* **86** (2012) 014023 [1111.5000].

[66] Y. Grossman and S. Schacht, *The emergence of the $\Delta U = 0$ rule in charm physics*, *JHEP* **07** (2019) 020 [1903.10952].

[67] W. Altmannshofer, R. Primulando, C.-T. Yu and F. Yu, *New Physics Models of Direct CP Violation in Charm Decays*, *JHEP* **04** (2012) 049 [1202.2866].

[68] J. Brod, A. L. Kagan and J. Zupan, *Size of direct CP violation in singly Cabibbo-suppressed D decays*, *Phys. Rev. D* **86** (2012) 014023 [1111.5000].

[69] Y. Grossman, A. L. Kagan and Y. Nir, *New physics and CP violation in singly Cabibbo suppressed D decays*, *Phys. Rev. D* **75** (2007) 036008 [hep-ph/0609178].

[70] UTfit collaboration, *The 2004 UTfit collaboration report on the status of the unitarity triangle in the standard model*, *JHEP* **07** (2005) 028 [hep-ph/0501199].